This is the peer-reviewed, final accepted version for American Mineralogist, published by the Mineralogical Society of America.
The published version is subject to change. Cite as Authors (Year) Title. American Mineralogist, in press.
DOI: https://doi.org/10.2138/am-2023-9150. http://www.minsocam.org/

Revision 3

Thermal equation of state of Li-rich schorl up to 15.5 GPa and 673 K: Implications for lithium and boron transport in slab subduction

WEI CHEN [1,2,3], SHANRONG ZHANG [1,2], MENGZENG WU [1,2], QIFA ZHONG [1,2], SHIJIE HUANG [1,2], KAI WANG [1,2], WEI ZHAO [1,2], JINGUI XU [1,*], DAWEI FAN [1], WENGE ZHOU [1]

[1] *Key Laboratory of High-Temperature and High-Pressure Study of the Earth's Interior, Institute of Geochemistry, Chinese Academy of Sciences, Guiyang, Guizhou 550081, China*

[2] *University of Chinese Academy of Sciences, Beijing 100049, China*

[3] *Guizhou Polytechnic of Construction, Guiyang, Guizhou 551400, China*

* Corresponding Author: Jingui Xu (xujingui@vip.gyig.ac.cn)

ABSTRACT: The thermal equation of state (EoS) of natural schorl has been established at high temperatures up to 673 K and high pressures up to 15.5 GPa using *in-situ* synchrotron X-ray diffraction combined with a diamond anvil cell. The pressure-volume (*P-V*) data were fitted to the third-order Birch-Murnaghan EoS with V_0 = 1581.45 ± 0.25 Å^3, K_0 = 111.6 ± 0.9 GPa and K'_0 = 4.4 ± 0.2; additionally, when K'_0 was fixed at a value of 4, V_0 = 1581.04 ± 0.20 Å^3 and K_0 = 113.6 ± 0.3 GPa. The V_0 (1581.45 ± 0.25 Å^3) obtained by the third-order Birch-Murnaghan EoS agreed well with the measured V_0 (1581.45 ± 0.05 Å^3) under ambient conditions; this result confirmed the high accuracy of the experimental data in this study. Furthermore, the axial compression data of the schorl at room temperature were also fitted to a "linearized" third-order Birch-Murnaghan EoS, and the obtained axial moduli for the *a*- and *c*-axes were K_a = 621 ± 9 GPa and K_c = 174 ± 2 GPa, respectively. Consequently, the axial compressibilities were β_a = 1.61×10^{-3} GPa^{-1} and β_c = 5.75×10^{-3} GPa^{-1} with an anisotropic ratio of β_a:β_c = 0.28:1.00, indicating axial compression anisotropy. In addition, the compositional effect on the axial

This is the peer-reviewed, final accepted version for American Mineralogist, published by the Mineralogical Society of America.
The published version is subject to change. Cite as Authors (Year) Title. American Mineralogist, in press.
DOI: https://doi.org/10.2138/am-2023-9150. http://www.minsocam.org/

compressibilities of tourmalines was also discussed. Fitting our pressure-volume-temperature (*P-V-T*) data to the high-temperature third-order Birch-Murnaghan EoS provided the following thermal EoS parameters: $V_0 = 1581.2 \pm 0.2$ Å^3, $K_0 = 110.5 \pm 0.6$ GPa, $K'_0 = 4.6 \pm 0.2$, $(\partial K_T/\partial T)_P = -0.012 \pm 0.003$ GPa K^{-1} and $\alpha_{V0} = (2.4 \pm 0.2) \times 10^{-5}$ K^{-1}. The obtained thermal EoS parameters in this study were also compared with those of previous studies on other tourmalines. The potential factors influencing the thermal EoS parameters of tourmalines were further discussed.

Keywords: Schorl; Equation of state; High pressure and high temperature; X-ray diffraction; Diamond anvil cell

INTRODUCTION

Tourmaline is the most abundant and widespread borosilicate mineral on Earth. It forms over a wide range of temperature and pressure conditions, and typically occurs in a wide variety of granites, granitic pegmatites, sedimentary, metamorphic rocks, and even (ultra)high pressure metamorphic rocks (Slack 1996; Dutrow and Henry 2011; van Hinsberg et al. 2011; Nabelek 2021; Ertl et al. 2022; Han et al. 2023; Vincent et al. 2023). Therefore, tourmaline is stable in environments that extend from the crust to ultrahigh pressure conditions prevailing in the upper mantle (Ota et al. 2008; Dutrow and Henry 2011; van Hinsberg et al. 2011; Henry and Dutrow 2012) and can maintain equilibrium with a variety of geological fluids (Meyer et al. 2008; Konzett et al. 2012; Berryman et al. 2016). The diffusion rate of the main and trace elements in tourmaline is extremely low (van Hinsberg et al. 2011); thus, tourmaline may preserve textural, compositional, and isotopic features during growth and hence reveal considerable details regarding its crystallized environment (e.g., Maloney et al. 2008; van Hinsberg et al. 2011; Berryman et al. 2017; Kotowski et al. 2020; Qiu et al. 2021; Feng et al. 2022; Li et al. 2022; Guo et al. 2023). More importantly, as a dominant carrier of light elements (e.g., lithium and boron), tourmaline plays a vital role in the lithium and boron cycles in the deep Earth, especially in subduction zones (e.g., Nakano and Nakamura 2001; Bebout and Nakamura 2003; Ota et al. 2008; van Hinsberg et al. 2011; Liu and Jiang 2021; Srivastava and Singh 2022). Thus, studies

Always consult and cite the final, published document. See http:/www.minsocam.org or GeoscienceWorld

of the thermal stability and equation of state (EoS) of tourmaline in the subduction slab can aid in the assessment of the lithium and boron cycle depth and explain the formation of lithium deposits.

Tourmaline is a kind of ring-silicate mineral, and its structure can be expressed as $XY_3Z_6T_6O_{18}(BO_3)_3V_3W$, where X = Na^+, K^+, Ca^{2+}, vacancy; Y = Mg^{2+}, Fe^{2+}, Al^{3+}, Li^+, Fe^{3+}, Cr^{3+}, V^{3+}, Mn^{2+}; Z = Al^{3+}, Fe^{3+}, Cr^{3+}, V^{3+}, Mg^{2+}, Fe^{2+}; T = Si^{4+}, Al^{3+}, B^{3+}; B = B^{3+}; V = $(OH)^-$, O^{2-}; W = $(OH)^-$, F^-, O^{2-} (Hawthorne and Henry 1999; Henry et al. 2011). Tourmaline has a trigonal crystal system and belongs to the *R*3*m* space group (Fig. 1). Its structure consists of two alternating basic structural layers. One consists of sixfold rings of tetrahedra (*T* sites) with a threefold axis along the *c* direction. The other consists of octahedral clusters on top of the tetrahedral rings, with three inner *Y* sites and six outer *Z* sites arranged concentrically. The *X* site occupies a nine-coordinate polyhedron above the center of the sixfold ring. B atoms form $[BO_3]^{3-}$ triangles linked to the *Y*- and *Z*-octahedra, almost perpendicular to the *c*-axis.

The chemical composition of tourmaline is diverse, and there are many isomorphic substituents in its structure (Hawthorne and Henry 1999; Bosi et al. 2022). The physical properties of tourmaline, such as the intrinsic dipole moment (Kim et al. 2018) and bulk modulus (Berryman et al. 2019; Chen et al. 2022), depend on the type of cation at the *X*, *Y*, and *Z* positions. Schorl (Fe-rich tourmaline) is the most common in the tourmaline supergroup, occurring in pegmatites and granites (e.g., Novák et al. 2004; Filip et al. 2012; Chakraborty 2021; Zhao et al. 2022). In addition, schorl is also an important petrogenetic indicator due to its ubiquity and sensitivity to fO_2 conditions (e.g., Foit et al. 1989; Fuchs et al. 2002; Pieczka and Kraczka 2004).

To date, pressure-volume (*P*-*V*) EoS studies of tourmalines (e.g., uvite, dravite, schorl, maruyamaite, magnesio-foitite, olenite, and elbaite) have been widely carried out using synchrotron X-ray diffraction (XRD) combined with a diamond anvil cell (e.g., Li et al. 2004; Xu et al. 2016; O'Bannon III et al. 2018; Berryman et al. 2019; Likhacheva et al. 2019; Chen et al. 2022). For instance, Li et al. (2004) performed the first *in situ* high-pressure synchrotron energy-dispersive XRD experiments on a natural schorl up to 27.8 GPa using a methanol-ethanol-water mixture (16:3:1) as the

This is the peer-reviewed, final accepted version for American Mineralogist, published by the Mineralogical Society of America.
The published version is subject to change. Cite as Authors (Year) Title. American Mineralogist, in press.
DOI: https://doi.org/10.2138/am-2023-9150. http://www.minsocam.org/

pressure medium. They obtained a bulk modulus K_0 = 184(4) GPa with a fixed pressure derivative of K'_0 = 4. However, O'Bannon III et al. (2018) conducted synchrotron single-crystal XRD measurements on a natural dravite at high pressures up to ~24 GPa using neon as the pressure medium and obtained K_0 = 109.6(3.2) GPa and K'_0 = 4.6(8). The K_0 of dravite obtained by O'Bannon III et al. (2018) is significantly less than that of schorl obtained by Li et al. (2004). Later, Likhacheva et al. (2019) studied the compressibility of natural maruyamaite using synchrotron XRD up to 20 GPa with a helium pressure medium, and the obtained K_0 = 112(3) GPa was also clearly less than that of Li et al. (2004). In addition, Berryman et al. (2019) collected synchrotron single-crystal XRD patterns of five synthetic Mg-Al tourmalines (dravite, K-dravite, magnesio-foitite, oxy-uvite, and olenite) at high-pressures up to 60 GPa with a neon pressure medium, and the reported K_0 ranged from 97(6) GPa to 116(6) GPa. Moreover, Chen et al. (2022) recently investigated the EoS of natural elbaite using *in situ* synchrotron XRD at high pressures up to 21.1 GPa with a neon pressure medium and concluded that the reasonable range of K_0 for tourmalines was 106-128 GPa. Therefore, the K_0 of the schorl reported by Li et al. (2004) seems abnormally high and unreasonable. However, further studies on the EoS are needed to resolve this discrepancy.

To the best of our knowledge, few experimental studies on the pressure-volume-temperature (*P-V-T*) EoS of tourmaline under high pressure and high temperature conditions are available. To date, the only previous *P-V-T* EoS study of tourmaline was by Xu et al. (2016), who tested a natural uvite up to 18 GPa and 723 K and obtained its thermal EoS parameters. However, the *P-V-T* EoS of other tourmalines has not yet been reported. Thus, additional *P-V-T* EoS studies on tourmalines with different compositions are needed to evaluate the compositional influence on the thermal EoS parameters (Fan et al. 2015b; Ye et al. 2019; Li et al. 2022; Xu et al. 2020, 2022a).

In this study, we investigated the *P-V-T* relationships of schorl up to 15.5 GPa and 673 K, using a diamond anvil cell combined with *in situ* synchrotron XRD. First, the compressibility of the schorl under room temperature and high pressure conditions

Always consult and cite the final, published document. See http:/www.minsocam.org or GeoscienceWorld

This is the peer-reviewed, final accepted version for American Mineralogist, published by the Mineralogical Society of America.
The published version is subject to change. Cite as Authors (Year) Title. American Mineralogist, in press.
DOI: https://doi.org/10.2138/am-2023-9150. http://www.minsocam.org/

was determined. In addition, we compared the compressibility of schorl and elbaite, and analyzed the possible influencing factors. Moreover, the anisotropic linear compressibilities of schorl and elbaite were also discussed. Finally, the thermal EoS properties of the schorl were obtained by fitting the *P-V-T* data to the high temperature Birch-Murnaghan EoS. Our results were also compared with those of previous studies on other tourmalines.

SAMPLE AND EXPERIMENT

The tourmaline selected in this study is a natural sample with a good columnar crystal morphology. Chemical analyses (Table 1) were carried out by various methods, including electron probe microanalysis (EPMA) and laser ablation inductively coupled plasma mass spectrometry (LA-ICP-MS).

The chemical composition of the tourmaline sample was determined by EMPA with a JEOL JXA-8230 instrument using a 15 kV accelerating voltage, a 20 nA beam current, and a beam diameter of 5 μm. The element peaks and backgrounds were measured for all elements with counting times of 10 s and 5 s, respectively. The following standards were used: hornblende (SiO_2, TiO_2, MgO, CaO, Na_2O, K_2O, and Al_2O_3), gahnite (ZnO), olivine (NiO), pyrope (FeO, MnO, and Cr_2O_3) and fluorite (F). The data were reduced online using the ZAF program. More detailed experimental conditions for the EMPA measurements are reported by Chen et al. (2022, 2023).

Because some significant components (e.g., Li, B and H_2O) cannot be directly determined by EMPA, the concentrations of Li and B in the tourmaline sample were investigated by LA-ICP-MS at the State Key Laboratory of Ore Deposit Geochemistry, Institute of Geochemistry, Chinese Academy of Sciences. An Agilent 7500 ICP-MS instrument was connected to a GeoLas Pro 193-nm ArF excimer laser ablation system. A beam diameter of 15 μm with a laser repetition rate of 10 Hz was used. Helium was used as the carrier gas and was mixed with argon via a T-connector before entering the ICP-MS instrument. The glass standard NIST610 was used for external calibration. More detailed analysis conditions are reported by Tang et al. (2020).

Always consult and cite the final, published document. See http:/www.minsocam.org or GeoscienceWorld

This is the peer-reviewed, final accepted version for American Mineralogist, published by the Mineralogical Society of America.
The published version is subject to change. Cite as Authors (Year) Title. American Mineralogist, in press.
DOI: https://doi.org/10.2138/am-2023-9150. http://www.minsocam.org/

Previous studies have shown that the OH content can be relatively accurately determined by the charge balance (e.g., Henry et al. 2002). Thus, the amount of OH^- at the *V*- and *W*-sites can be evaluated from bond valence sum calculations. The Windows program WinTcac developed by Yavuz et al. (2014) was used to calculate the chemical formula of the tourmaline sample from the EMPA and LA-ICP-MS data. In this study, the OH content was calculated by considering OH + O + F = 4 apfu and *V* = OH = 3 apfu. The estimated chemical formula was $(Na_{0.75}Ca_{0.04}K_{0.01}\square_{0.20})(Al_{0.78}Li_{0.74}Fe_{1.32}Mn_{0.04}Mg_{0.08}Zn_{0.01}Ti_{0.03})Al_6Si_{6.09}O_{18}(BO_3)_3(OH)_3(OH_{0.27}F_{0.03}O_{0.70})$, where □ indicates vacancy. Finally, the species of the tourmaline sample was additionally verified by the spreadsheet of Henry et al. (2011), and the chemical composition corresponded to the schorl species (Li-rich schorl).

The pure schorl mineral grains were selected by hand under a microscope and then ground under ethanol in an agate mortar for 4-6 h to an average grain size of ~10 μm. The ground samples were heated at 100 °C in a constant temperature furnace for 2 h to eliminate the absorbed water before being used in the subsequent synchrotron XRD experiments.

High pressure and high temperature experiments were carried out by using a modified Merrill-Bassett diamond anvil cell with a pair of 500 μm culet-size diamond anvils. The sample chamber was prepared from a rhenium gasket with a preindented thickness of ~60 μm and a 300 μm-diameter hole in the center of the indented region. The schorl powder was mixed with 3 wt.% platinum powder as the pressure calibrant by mechanically grinding the mixture for approximately 2 h. Subsequently, the mixture was lightly pressed between two opposing diamond anvils to form an approximately 25 μm thick disk, and a piece of the pressed sample approximately 100 μm in diameter was loaded into the sample chamber. A methanol-ethanol-water mixture (16:3:1) was used as the pressure transmitting medium. The pressure was determined using the thermal EoS of platinum (pressure marker) (Fei et al. 2007). Heating was carried out by using a resistance-heating system, and the temperature was measured by a $Pt_{90}Rh_{10}$-Pt_{100} thermocouple attached to one of the diamond anvils

Always consult and cite the final, published document. See http:/www.minsocam.org or GeoscienceWorld

This is the peer-reviewed, final accepted version for American Mineralogist, published by the Mineralogical Society of America.
The published version is subject to change. Cite as Authors (Year) Title. American Mineralogist, in press.
DOI: https://doi.org/10.2138/am-2023-9150. http://www.minsocam.org/

approximately 500 μm away from the diamond culet. The resistance-heating system provides a stable and uniform temperature distribution within the pressure chamber and reliable temperature control by means of a thermocouple. Moreover, the exceptional thermal conductivity of the diamond anvil has the major advantage of transferring heat to the sample inside the pressure chamber. Thus, obtaining a stable and uniform temperature distribution within the pressure chamber highly depends on the stabilization time at high temperature and the tightness of the thermocouple glued to the diamond. Thus, to ensure that the thermocouple correctly reflected the temperature of the sample chamber, we tightly glued the thermocouple to the diamond. Each *in situ* XRD pattern was collected after the experimental temperature was maintained for 600 s for temperature stability. The temperatures of the sample chamber were actively stabilized using a temperature controller with a self-tuning function, and the fluctuation temperature displayed by the temperature controller was within ±1 K. The exposure time for collecting diffraction patterns of the sample was 600 s. Details of the experimental setup and cell assembly were described in previously published articles (e.g., Fan et al. 2010).

In situ high pressure and high temperature angle-dispersive XRD experiments were conducted at the 4W2 beamline of the Beijing Synchrotron Radiation Facility (BSRF). A Pilatus detector was used to collect diffraction patterns. The wavelength of the monochromatic X-ray beam was 0.6199 (1) Å, which was calibrated by scanning through the Mo metal *K*-absorption edge. The beam size was focused to 20 × 30 μm^2 by a pair of Kirkpatrick-Baez mirrors (Kirkpatrick and Baez 1948). The tilting and rotation of the detector relative to the incident X-ray beam were calibrated using cerium dioxide (CeO_2) powder as the XRD standard. The sample-detector distance was calculated from the powder CeO_2 diffraction pattern under ambient conditions.

The diffraction patterns were integrated to generate conventional one-dimensional profiles using the *Fit2D* program (Hammersley et al. 1996). The diffraction peak positions were fitted by *Origin* 8.5 software. The unit-cell parameters and volumes were calculated using *UnitCell* software (Holland and Redfern 1997).

Always consult and cite the final, published document. See http:/www.minsocam.org or GeoscienceWorld

This is the peer-reviewed, final accepted version for American Mineralogist, published by the Mineralogical Society of America.
The published version is subject to change. Cite as Authors (Year) Title. American Mineralogist, in press.
DOI: https://doi.org/10.2138/am-2023-9150. http://www.minsocam.org/

RESULTS

The typical XRD patterns of the schorl at various pressures and temperatures are shown in Figure 2. With increasing pressure at different temperatures (Fig. 2), all peaks shifted toward higher 2θ angles. Moreover, the number of peaks in the diffraction data of the schorl sample did not change over the experimental pressure-temperature range (Fig. 2), indicating that no structural transition occurred. The unit-cell parameters and volumes of the schorl at various pressure and temperature conditions are listed in Tables 2 and 3. Figures 3 and 4 show the volumetric and axial compression of the schorl in this study. In addition, the XRD data collected under ambient conditions yielded the unit-cell parameters and volumes of a_0 = 15.9532 (3) Å, c_0 = 7.1751 (3) Å, and V_0 = 1581.45 (5) Å^3.

We first fitted the *P-V* data collected at the 300 K isotherm to the room-temperature Birch-Murnaghan EoS. Then, we employed another common method, the high-temperature Brich-Murnaghan EoS approach, to derive the thermal EoS parameters from the measured *P-V-T* data.

Room-temperature Birch-Murnaghan equation of state

The pressure-volume (*P-V*) relationships were determined by fitting the room temperature data to a third-order Birch-Murnaghan EoS, which is represented as follows (Birch 1947):

$$P = (3/2)K_0[(V_0/V)^{7/3}-(V_0/V)^{5/3}]\times\{1+(3/4)(K'_0-4)[(V_0/V)^{2/3}-1]\} \quad (1)$$

where V_0, K_0, and K'_0 are the zero-pressure unit-cell volume, zero-pressure isothermal bulk modulus and its pressure derivative, respectively. Analyses of Eq. (1) by the *EoSFit* program (Angel et al. 2014; Gonzalez-Platas et al. 2016) with all parameters free yielded: V_0 = 1581.45 ± 0.25 Å^3, K_0 = 111.6 ± 0.9 GPa, and K'_0 = 4.4 ± 0.2 (Table 4). The refined value of V_0 (1581.45 (25) Å^3) was within approximately 1σ compared with the V_0 (1581.45 (5) Å^3) measured by XRD under ambient conditions; this indicated the excellent accuracy of the refined results (Angel 2000). With K'_0 fixed at 4, the results were V_0 = 1581.04 ± 0.20 Å^3, and K_0 = 113.6 ± 0.3 GPa. In addition, with V_0 fixed at 1581.45 Å^3, the results were K_0 = 111.6 ± 0.4 GPa, and K'_0 = 4.4 ± 0.1.

Always consult and cite the final, published document. See http:/www.minsocam.org or GeoscienceWorld

This is the peer-reviewed, final accepted version for American Mineralogist, published by the Mineralogical Society of America.
The published version is subject to change. Cite as Authors (Year) Title. American Mineralogist, in press.
DOI: https://doi.org/10.2138/am-2023-9150. http://www.minsocam.org/

To evaluate the quality of our third-order Birch-Murnaghan EoS fitting, the relationship between the Eulerian definition of finite strain f_E ($f_E = [(V_0/V)^{2/3}-1]/2$) and the "normalized stress" F_E ($F_E = P/3f_E(1+2f_E)^{5/2}$) (Birch 1978) is plotted and shown in Figure 5a. The weighted linear fit of the data points yielded an intercept value of $F_{EV}(0)$ = 111.9 (4) GPa, which was in good agreement with the isothermal bulk modulus obtained by the third-order Birch-Murnaghan EoS (K_0 = 111.6 (9) GPa). Moreover, the functions of F_E and f_E had a slightly positive slopes, indicating that K'_0 was greater than 4; this results was consistent with K'_0 = 4.4 (2) from the third-order Birch-Murnaghan EoS. Therefore, the obtained EoS parameters from the third-order Birch-Murnaghan EoS fitting are a reasonable description of the *P-V* data in this study.

The normalized unit-cell parameters (a/a_0 and c/c_0) of schorl at room temperature are plotted as a function of pressure in Figure 4. By fitting the unit-cell parameters of the schorl at room temperature using a "linearized" third-order Birch-Murnaghan EoS with the *EosFit* program (Angel et al. 2014; Gonzalez-Platas et al. 2016), the obtained a_0 and c_0 are 15.9532 (3) Å and 7.1751 (3) Å, respectively. The refined unit-cell parameters are consistent with the results obtained from the XRD measurements under ambient conditions in this study due to their uncertainties (Table 2). The refined linear moduli and their pressure derivatives are K_a = 621 (9) GPa, K_c = 174 (2) GPa and K'_a =16 (3), K'_c = 8.7 (5), respectively. In addition, the weighted linear fit of the F_E-f_E data points yields intercepts of $F_{Ea}(0)$ = 620 (6) GPa for the *a*-axis and $F_{Ec}(0)$ = 174 (1) GPa for the *c*-axis; these results effectively agree with the results from the "linearized" third-order Birch-Murnaghan EoS. Moreover, the slopes obtained from the linear fits of the F_E-f_E plots are positive for the *a*-axis and negative for the *c*-axis (Figs. 5b and 5c). The results are in good agreement with $K'_a > 12$ and $K'_c < 12$ from the "linearized" third-order Birch-Murnaghan EoS fits.

The axial compressibility β_l under ambient conditions has the following form (Angel et al. 2014):

$$\beta_l = 1/K_l \quad (2)$$

Always consult and cite the final, published document. See http:/www.minsocam.org or GeoscienceWorld

This is the peer-reviewed, final accepted version for American Mineralogist, published by the Mineralogical Society of America.
The published version is subject to change. Cite as Authors (Year) Title. American Mineralogist, in press.
DOI: https://doi.org/10.2138/am-2023-9150. http://www.minsocam.org/

In analyses using Eq. (2) with K_l, we obtained the compressibility of the *a*- and *c*-axes and they were determined to be 1.61×10^{-3} GPa^{-1} and 5.75×10^{-3} GPa^{-1}, respectively; these results indicated that schorl has axial compressive anisotropy. The *c*-axis of the schorl was 3.57 times more compressible than the *a*-axis under ambient conditions (Fig. 4).

High-temperature Birch-Murnaghan equation of state

The *P-V-T* data (Table 3) were used to determine the thermal EoS parameters of schorl up to ~15.50 GPa and 673 K. The third-order Birch-Murnaghan EoS was applied to our high pressure and high temperature data as follows:

$$P = (3/2)K_{T0}[(V_{T0}/V)^{7/3}-(V_{T0}/V)^{5/3}]\times\{1+(3/4)(K'_{T0}-4)[(V_{T0}/V)^{2/3}-1]\} \quad (3)$$

In this equation, the thermal dependences of the zero-pressure unit-cell volume V_{T0} and bulk modulus K_{T0} at different isotherms are expressed using the following equations:

$$V_{T0} = V_0 \exp\int_{300}^{T} \alpha_T dT \quad (4)$$

$$K_{T0}=K_0+(\partial K_T/\partial T)_P\times(T-300) \quad (5)$$

where V_0 is the volume at zero-pressure and room-temperature, and the temperature derivative of V_{T0} can be estimated by a function of the thermal expansion α_T (Eq. 4). The thermal dependence of the bulk modulus K_{T0} is expressed by a linear function of temperature (Eq. 5), assuming that the temperature derivative $(\partial K_T/\partial T)_P$ is constant in the temperature range of this study.

The obtained thermal EoS parameters α_{V0}, $(\partial K_T/\partial T)_P$, K_0 and K'_0 for the schorl in this study are shown in Table 4, and are compared with those from other tourmalines in previous studies. Fitting of the *P-V-T* data to the high-temperature third-order Birch-Murnaghan EoS yields the following results for the schorl: $V_0 = 1581.2 \pm 0.2$ Å^3, $K_0 = 110.5 \pm 0.6$ GPa, $K'_0 = 4.6 \pm 0.2$, $(\partial K_T/\partial T)_P = -0.012 \pm 0.003$ GPa K^{-1} and $\alpha_{V0} = (2.4 \pm 0.2) \times 10^{-5}$ K^{-1}. The obtained V_0, K_0 and K'_0 determined here are very consistent with those from the *P-V* data fitting at 300 K within their uncertainties. The measured unit-cell volumes are plotted in Figure 6 as a function of pressure together with the isotherms calculated using the thermal EoS parameters derived from the current fits;

Always consult and cite the final, published document. See http:/www.minsocam.org or GeoscienceWorld

This is the peer-reviewed, final accepted version for American Mineralogist, published by the Mineralogical Society of America.
The published version is subject to change. Cite as Authors (Year) Title. American Mineralogist, in press.
DOI: https://doi.org/10.2138/am-2023-9150. http://www.minsocam.org/

the results show good agreement between the fit and the measured *P-V-T* data.

DISCUSSION

The *P-V* EoS of various tourmalines (e.g., uvite, dravite, maruyamaite, foitite, olenite, and elbaite) has been investigated in previous high-pressure XRD experiments, but *P-V* EoS studies on schorl are limited. To date, only Li et al. (2004) reported the *P-V* EoS of schorl, they measured the compressibility of a natural tourmaline (schorl) at high pressures up to 27.8 GPa using the synchrotron XRD method. Although they did not characterize the composition of their tourmaline sample, they reported that the natural tourmaline sample was schorl (Li et al. 2004). They used a methanol-ethanol-water (at a ratio of 16:3:1) pressure medium and obtained an unusually high K_0 value of 184 (4) GPa (with fixed K'_0 = 4). In contrast, the obtained K_0 (113.6 (3) GPa) of schorl in this study (with fixed K'_0 = 4) is ~38% lower. From Figures 3 and 4, the volumetric and axial compression of the schorl from Li et al. (2004) is not only very scattered and irregular but also significantly greater than the volumetric and axial compression of the schorl in this study and of the elbaite in the study by Chen et al. (2022). Notably, the experimental maximum pressure (~27.8 GPa) from the study by Li et al. (2004) greatly exceeded the hydrostatic pressure condition (~10.5 GPa) of their pressure medium (Angel et al. 2007; Klotz et al. 2009a). Thus the previously reported K_0 = 184 (4) GPa by Li et al. (2004) should be considered unreasonable and inaccurate.

In this study, we also used a methanol-ethanol-water mixture with a ratio of 16:3:1 for the pressure media. This pressure medium solidifies at pressures above ~10.5 (± 0.5) GPa, and therefore the hydrostatic pressure environment in the sample chamber may be significantly influenced (Angel et al., 2007; Klotz et al. 2009a). However, we did not collect data far above the hydrostatic limit of the pressure medium, as in Li et al. (2004). In addition, previous studies have demonstrated that the hydrostatic limits can be considerably increased by modest heating (Klotz et al. 2009b). Thus, the sample chamber in this study was heated to 673 K at pressures for the relaxation of deviatoric stress (Fan et al. 2017b). Furthermore, to evaluate the possible influence of

Always consult and cite the final, published document. See http:/www.minsocam.org or GeoscienceWorld

This is the peer-reviewed, final accepted version for American Mineralogist, published by the Mineralogical Society of America.
The published version is subject to change. Cite as Authors (Year) Title. American Mineralogist, in press.
DOI: https://doi.org/10.2138/am-2023-9150. http://www.minsocam.org/

nonhydrostatic conditions on the *P-V-T* EoS fitting results, we also fitted the *P-V-T* EoS of schorl after removing the experimental data with pressures greater than ~12 GPa, and obtained the following results for the schorl: V_0 = 1581.4 ± 0.5 Å^3, K_0 = 111.5 ± 1.5 GPa, K'_0 = 4.6 ± 0.3, $(\partial K_T/\partial T)_P$ = -0.009 ± 0.003 GPa K^{-1} and α_{V0} = (2.1 ± 0.2) × 10^{-5} K^{-1}. These values are very consistent with all the *P-V-T* data fitting results within their uncertainties (Table 4). Based on the above analysis, we deduce that the sample chamber in this study maintains a good hydrostatic pressure environment at pressures up to 16.05 GPa.

Recently Chen et al. (2022) summarized the results from previous experiments and discussed in detail the potential factors behind the discrepancies in K_0 and K'_0 among tourmalines. They concluded that the different pressure media, K'_0 values and mineral compositions could all contribute to the discrepancies in the reported bulk moduli of tourmalines. They further inferred that excluding the influence of external factors such as the pressure medium, reasonable ranges of K_0 and K'_0 could be 106-128 GPa and 3.5-5.0, respectively. The obtained K_0 (111.6 (9) GPa) and K'_0 (4.4 (2)) of the schorl in this study are both within the aforementioned range. Thus the above analysis not only indicates that our results are more reasonable but also further confirms the reliability of the K_0 and K'_0 ranges summarized by Chen et al. (2022). In addition, there are similarities between the composition of tourmaline in this study and that of Chen et al. (2022); specifically, both are Li- and Fe-bearing tourmaline. Thus, the obtained *P-V* EoS parameters of the schorl in this study and those of the elbaite from Chen et al. (2022) enable the further exploration the compositional influence (e.g., Fe or Li) on the volumetric and axial compressibilities of Li-bearing tourmalines.

Table 4 also shows that the K_0 and K'_0 of the elbaite reported by Chen et al. (2022) are ~2.8% and ~4.5% greater than those of the schorl in this study, respectively. In static compression studies, a trade-off exists between the fitted K_0 and K'_0, which are negatively correlated. Considering the correlation between K_0 and K'_0 in an EoS fit, we cannot only compare K_0 and neglect the K'_0. Thus, to accurately evaluate the difference between the K_0 values obtained in this study and those reported by Chen et al. (2022), we compared the results with a fixed K'_0 value of 4.0. From Table 4, the K_0

Always consult and cite the final, published document. See http:/www.minsocam.org or GeoscienceWorld

This is the peer-reviewed, final accepted version for American Mineralogist, published by the Mineralogical Society of America.
The published version is subject to change. Cite as Authors (Year) Title. American Mineralogist, in press.
DOI: https://doi.org/10.2138/am-2023-9150. http://www.minsocam.org/

values of this study and Chen et al. (2022) with a fixed K'_0 of 4.0 are 113.6(3) GPa and 116.4(4) GPa, respectively. The obtained K_0 in this study for schorl is ~2.4% lower than that reported by Chen et al. (2022).

By carefully examining the composition characteristics of elbaite [$(Na_{0.62}Ca_{0.04}\square_{0.34})(Al_{1.90}Li_{0.98}Fe_{0.09}Mn_{0.02})Al_6Si_6O_{18}(BO_3)_3(OH)_3(OH_{0.20},F_{0.48},O_{0.32})$] from Chen et al. (2022) and schorl $(Na_{0.75}Ca_{0.04}K_{0.01}\square_{0.20})(Al_{0.78}Li_{0.74}Fe_{1.32}Mn_{0.04}Mg_{0.08}Zn_{0.01}Ti_{0.03})Al_6Si_{6.09}O_{18}(BO_3)_3(OH)_3(OH_{0.27}F_{0.03}O_{0.70})$ in this study, the *X* sites in these samples are relatively simple. They are predominantly occupied by Na, some of them are vacant (□), and the other elements (e.g., Ca and K) are negligible. However, the compositional variation at the *X* site in tourmalines merely leads to changes in the neighboring O1–H1 bond without any identifiable changes in the lattice-bonding environment (Berryman et al. 2016). Thus, the *X*-site-occupying ion does not have a demonstrable effect on the compression behavior of tourmaline (Berryman et al. 2019; Chen et al. 2022).

However, in comparison to the simple compositional variation at the *X* site of these two tourmalines in this study and that reported by Chen et al. (2022), the compositional characteristics at the *Y* site are more complex. For the elbaite sample from Chen et al. (2022), the *Y* site is predominantly occupied by Al and Li, with a few other elements (e.g., Fe and Mn). In contrast, except for Al and Li, the schorl sample in this study contains a significant amount of Fe at the *Y* site. The effective ionic radii of Fe^{2+}(VI) (0.776 Å) are ~41.9% larger than those of Al^{3+}(VI) (0.547 Å) (Bosi 2018). As a consequence, the mean bond length of Fe^{2+}-O (2.1536 Å) at the *Y* site is ~13.1% greater than the mean bond length of Al^{3+}-O (1.9043) (Bačík and Fridrichová 2021). Accordingly, the bond strength of Fe^{2+}-O in the schorl is weaker than that of Al^{3+}-O. Therefore, the schorl exhibits greater compressibility and a smaller isothermal bulk modulus.

Thus, based on the above discussion, the bond strengths of Fe^{2+}-O at the *Y* site may mainly contribute to the different compressibilities between the schorl in this study and the elbaite in Chen et al. (2022). This reasoning is consistent with the conclusion

Always consult and cite the final, published document. See http:/www.minsocam.org or GeoscienceWorld

This is the peer-reviewed, final accepted version for American Mineralogist, published by the Mineralogical Society of America.
The published version is subject to change. Cite as Authors (Year) Title. American Mineralogist, in press.
DOI: https://doi.org/10.2138/am-2023-9150. http://www.minsocam.org/

of Chen et al. (2023), who suggested that the bond strengths of the corresponding bonds at the *Y* site likely have a significant effect on the expansibility of Li-bearing tourmaline. Furthermore, to the best of our knowledge, there have been only two previous studies on the *P-V* EoS of Fe-bearing tourmalines, one study by Chen et al. (2022) investigated the *P-V* EoS of Fe-bearing elbaite, while the other one by Likhacheva et al. (2019) examined the *P-V* EoS of Fe-bearing maruyamaite (K-tourmaline) with the composition of $(Na_{0.28}Ca_{0.19}K_{0.54})(Al_{1.17}Fe_{0.39}Mg_{1.3}Ti_{0.14})(Al_5Mg)[Si_{5.95}Al_{0.05}O_{18}](BO_3)_3(OH_{2.31}O_{1.69})$. Thus, in this study, based on the obtained *P-V* EoS of the schorl and combining our results with the *P-V* EoS of previous studies (Likhacheva et al. 2019; Chen et al. 2022), we constructed a relationship between the K_0 values and the Fe content at the *Y* site of Fe-bearing tourmalines (Fig. 7). In addition, to accurately evaluate the influence of the Fe content on the K_0 of Fe-bearing tourmalines, we compared their K_0 values while keeping K'_0 fixed at 4.0. The K_0 of the Fe-bearing tourmalines shows a linear relationship with the Fe content. Within the experimental uncertainties, K_0 decreases linearly with increasing Fe content (Fig. 7):

$$K_0 = 116.59\ (0.05) - 6.8\ (0.1)\ X_{Fe}\ (R^2 = 0.999) \quad (6)$$

where X_{Fe} = Fe / (Fe + Mg + Li + Al) is the Fe content at the *Y* site of the tourmalines. Thus, the above equation further indicates that the bond strength of Fe^{2+}-O at the *Y* site likely has a significant effect on the compressibility of Fe-bearing tourmaline.

The axial compressibility of the schorl in this study indicates that the *c*-axis is softer than the *a*-axis. The calculated axial compressibilities are $\beta_a = 1.61\times10^{-3}$ GPa^{-1} and $\beta_c = 5.75\times10^{-3}$ GPa^{-1}, resulting in an anisotropic ratio of β_a:β_c = 0.28:1.00. Thus, our results reinforce the highly anisotropic elasticity of tourmaline. Similar anisotropic compression behaviors have been reported for natural elbaite, dravite, uvite, maruyamaite, and synthetic Mg-Al tourmalines (Xu et al. 2016; O'Bannon III et al. 2018; Berryman et al. 2019; Likhacheva et al. 2019; Chen et al. 2022). There are two possible reasons for the anisotropic compression behaviors of tourmalines with $\beta_c > \beta_a$ (Chen et al. 2022). One reason is the incorporation of relatively larger water

Always consult and cite the final, published document. See http:/www.minsocam.org or GeoscienceWorld

This is the peer-reviewed, final accepted version for American Mineralogist, published by the Mineralogical Society of America.
The published version is subject to change. Cite as Authors (Year) Title. American Mineralogist, in press.
DOI: https://doi.org/10.2138/am-2023-9150. http://www.minsocam.org/

molecules in the *c*-parallel structural channels of tourmalines (Bosi 2018). Another reason is that the [Si_6O_{18}] rings and cationic octahedral layers are arranged in the *c*-axis direction of tourmalines, which can be refilled with larger cations with large voids (Bosi and Lucchesi 2007; Bosi 2018).

Furthermore, the obtained linear moduli of the schorl in this study and their pressure derivatives under ambient conditions are different from those reported for the elbaite (K_a = 201 (4) GPa, K_c = 60 (1) GPa and K'_a = 6.9 (4), K'_c = 2.8 (1)) by Chen et al. (2022). Based on the relevant analysis of a recent article (Basu et al. 2023), the evident difference between our results and those of Chen et al. (2022) is the formalism used in Chen et al. (2022) where the unit-cell parameters were cubed to obtain a nonexistent volume, and a bulk finite strain formalism was used to determine axial compressibility. Thus, we refitted the linear moduli and their pressure derivatives of elbaite using the data from Chen et al. (2022) by the "linearized" third-order Birch-Murnaghan EoS. The refitted results for elbaite are as follows (Table 5): K_a = 610 (8) GPa, K_c = 182 (1) GPa, K'_a = 20 (1), and K'_c = 8.2 (1).

From Table 5, within their uncertainties, the axial compressibility of the *a*-axis for the schorl in this study is similar to that of the elbaite in Chen et al. (2022), but the axial compressibility of the *c*-axis for the schorl is smaller than that of the elbaite (Fig. 4 and Table 5). These results indicate that the axial compressibility anisotropy of the schorl in this study is larger than that of elbaite. Considering that the *c*-axis of tourmaline is correlated with the ZO_6 octahedron, the substitution of Al by larger cations (e.g., Fe) at the *Y* site will reduce the strength of the ZO_6 octahedra along the *c*-axis and perturb the degree of puckering of the six-membered SiO_4 rings, resulting in greater compressibility along the *c*-axis direction. Thus, the lower axial compressibility along the *c*-axis of the schorl can be attributed to the reduced stiffness of the ZO_6 octahedra.

Table 4 also provides a comparison between the α_{V0} of the schorl obtained in this study and those from previous studies. The α_{V0} obtained by *P*-*V*-*T* EoS fitting in this study is ~49% greater than the α_{V0} obtained for the same schorl sample through *T*-*V*

Always consult and cite the final, published document. See http:/www.minsocam.org or GeoscienceWorld

This is the peer-reviewed, final accepted version for American Mineralogist, published by the Mineralogical Society of America.
The published version is subject to change. Cite as Authors (Year) Title. American Mineralogist, in press.
DOI: https://doi.org/10.2138/am-2023-9150. http://www.minsocam.org/

EoS fitting by Chen et al. (2023). Because both studies used the same tourmaline sample, the difference in the α_{V0} cannot be attributed to compositional variations.

Moreover, the obtained α_{V0} (4.39×10^{-5} K^{-1}) for a natural uvite from the *P*-*V*-*T* EoS fitted by Xu et al. (2016) is more than double or triple the α_{V0} derived from other investigations (α_{V0} = 1.34-2.05 × 10^{-5} K^{-1}) via *T*-*V* EoS fitting (Celata et al. 2021; Ballirano et al. 2022; Chen et al. 2023; Hovis et al. 2023). Excluding the compositional effects, the α_{V0} obtained by *P*-*V*-*T* EoS fitting (this study and Xu et al. 2016) is notably greater than that obtained by *T*-*V* EoS fitting. This phenomenon occurs not only in tourmalines but also in many other silicate minerals, such as pyroxene (Hovis et al. 2021; Ye et al. 2021; Xu et al. 2022b), garnet (Gréaux et al. 2011; Fan et al. 2017a), amphibole (Tribaudino et al. 2022), epidote (Li et al. 2021), clinohumite (Ye et al. 2013; Qin et al. 2017), topaz (Huang et al. 2020; Liu et al. 2023; Zhao et al. 2023), beryl (Fan et al. 2015a). There are likely two main reasons for this phenomenon. First, the thermal expansion coefficient α_T is dependent on the temperature range and temperature interval. Compared with *T*-*V* EoS fitting, the number of *T*-*V* data points at ambient pressure used for *P*-*V*-*T* EoS fitting is significantly lower. For instance, only five *V*-*T* data points between 298 and 673 K were used for *P*-*V*-*T* EoS fitting in this study. However, thirteen *T*-*V* data points between 298 and 663 K were used for *T*-*V* EoS fitting by Chen et al. (2023). Second, α_T and $(\partial K/\partial T)_P$ will affect each other in the processing of *P*-*V*-*T* EoS fitting. Thus, to obtain an accurate thermal expansion coefficient in future high pressure and high temperature XRD experiments, narrower temperature intervals and wider temperature ranges are needed (Liu et al. 2023).

Table 4 also shows a comparison of $(\partial K/\partial T)_P$ for schorl in this study with that for uvite by Xu et al. (2016). The $(\partial K/\partial T)_P$ obtained for schorl is in good agreement with that for uvite within their uncertainties (Table 4). Therefore, based on existing data, the $(\partial K/\partial T)_P$ of tourmalines may not be significantly affected by their composition; this reasoning is similar to the findings of some previous studies (e.g., Nishihara et al. 2005; Zou et al. 2012; Fan et al. 2015b) that considered that the $(\partial K/\partial T)_P$ for other silicate minerals exhibit similar values regardless of their mineral chemistry.

Always consult and cite the final, published document. See http:/www.minsocam.org or GeoscienceWorld

This is the peer-reviewed, final accepted version for American Mineralogist, published by the Mineralogical Society of America.
The published version is subject to change. Cite as Authors (Year) Title. American Mineralogist, in press.
DOI: https://doi.org/10.2138/am-2023-9150. http://www.minsocam.org/

IMPLICATIONS

In this study, we examined the thermal EoS and stability of schorl at high temperatures and pressures (up to 673 K and 16 GPa) using synchrotron radiation XRD. Depending on the exact chemistry of tourmaline, the expected thermodynamic stability of tourmaline ranged between 5-7 GPa at 500 °C, and between 800-1000 °C at 4 GPa (Ota et al. 2008; Dutrow and Henry 2011; van Hinsberg et al. 2011; Henry and Dutrow 2012).

Our results on the thermal EoS are vital thermodynamic data that can aid in the refinement of the *P*-*T* stability field of tourmaline. For full thermodynamic data, enthalpy, entropy, and heat capacity results are crucial and available for limited chemistry (Garofalo et al. 2000; Ogrodova et al. 2004; 2012). Tourmalines (e.g., schorl and uvite) likely have the potential to transport light elements into the Earth's interior via subduction zones and can release the light elements once they decompose as the geotherm intersects the *P*-*T* phase boundary. The released light elements accordingly affect the geochemical processes in the deep Earth (Nakano and Nakamura 2001; Bebout and Nakamura 2003; Zack et al. 2003; Bebout et al. 2007). For example, the breakdown of tourmaline can cause the release of boron, which largely influences the boron budget during the subduction of Earth's crust to mantle depths at convergent plate margins (Guo et al. 2022). Therefore, this potentially results in mantle B isotope anomalies near convergent margins (Nakano and Nakamura 2001). Moreover, in the subduction zones, as the pressure and temperature of the slab increase, the decomposition of the lithium-bearing minerals (e.g., tourmaline, phengite, and epidote) releases the fluxing elements such as lithium and fluorine, which can induce partial melting and form lithium-rich magmatism (e.g., Halama et al. 2009; Li et al. 2018; Liu et al. 2020). Simultaneously, weathering in arid areas in the hinterland of an orogenic belt can promote lithium enrichment in the basin, leading to the formation of lithium deposits (e.g., Sun et al. 2007; Chen et al. 2014).

ACKNOWLEDGMENTS AND FUNDING

We are thankful to Associate Editor Mainak Mookherjee and two anonymous

Always consult and cite the final, published document. See http:/www.minsocam.org or GeoscienceWorld

This is the peer-reviewed, final accepted version for American Mineralogist, published by the Mineralogical Society of America.
The published version is subject to change. Cite as Authors (Year) Title. American Mineralogist, in press.
DOI: https://doi.org/10.2138/am-2023-9150. http://www.minsocam.org/

reviewers for their valuable comments and advices which helped to improve the manuscript substantially. We also acknowledge Dr. Y.W. Tang for the LA-ICP-MS experiments assistance. This project was supported by National Natural Science Foundation of China (U2032118 and 42172048), Hundred Talents Program of the Chinese Academy of Sciences, Guizhou Provincial Science and Technology Projects (QKHPTRC-YQK[2023]035 and QKHJC-ZK[2021]ZD042), and Guizhou Provincial 2020 and 2021 Science and Technology Subsidies (Nos. GZ2020SIG and GZ2021SIG). The high-pressure and high-temperature XRD experiments were conducted at the 4W2 of the Beijing Synchrotron Radiation Facility (BSRF).

REFERENCES CITED

Angel, R.J. (2000) Equations of State. Reviews in Mineralogy & Geochemistry, 41, 35-59. https://doi.org/10.2138/rmg.2000.41.2

Angel, R.J., Bujak, M., Zhao, J., Gatta, G.D., and Jacobsen, S.D. (2007) Effective hydrostatic limits of pressure media for high-pressure crystallographic studies. Journal of Applied Crystallography, 40, 26-32. https://doi.org/10.1107/S0021889806045523

Angel, R.J., Gonzalez-Platas, J., and Alvaro, M. (2014) EosFit-7c and a Fortran module (library) for equation of state calculations. Zeitschrift für Kristallographie - Crystalline Materials, 229(5), 405-419. https://doi.org/10.1515/zkri-2013-1711

Bačík, P., and Fridrichová, J. (2021) Cation partitioning among crystallographic sites based on bond-length constraints in tourmaline-supergroup minerals. American Mineralogist, 106, 851-861. https://doi.org/10.2138/am-2021-7804

Ballirano, P., Celata, B., and Bosi, F. (2022) In situ high-temperature behaviour and breakdown conditions of uvite at room pressure. Physics and Chemistry of Minerals, 49, 40. https://doi.org/10.1007/s00269-022-01216-3

Basu, A., Mookherjee, M., Clapp, S., Chariton, S., and Prakapenka, V.B. (2023) High-pressure Raman scattering and X-ray diffraction study of kaolinite, $Al_2Si_2O_5(OH)_4$. Applied Clay Science, 245, 107144. https://doi.org/10.1016/j.clay.2023.107144

Always consult and cite the final, published document. See http:/www.minsocam.org or GeoscienceWorld

This is the peer-reviewed, final accepted version for American Mineralogist, published by the Mineralogical Society of America.
The published version is subject to change. Cite as Authors (Year) Title. American Mineralogist, in press.
DOI: https://doi.org/10.2138/am-2023-9150. http://www.minsocam.org/

Bebout, G.E., Bebout, A.E., and Graham, C.M. (2007) Cycling of B, Li, and LILE (K, Cs, Rb, Ba, Sr) into subduction zones: SIMS evidence from micas in high-P/T metasedimentary rocks. Chemical Geology, 239, 284-304. https://doi.org/10.1016/j.chemgeo.2006.10.016

Bebout, G., and Nakamura, E. (2003) Record in metamorphic tourmalines of subduction-zone devolatilization and boron cycling cycling record in metamorphic tourmalines of subduction-zone devolatilization and boron cycling. Geology, 31, 407-410. https://doi.org/10.1130/0091-7613(2003)031<0407:RIMTOS>2.0.CO;2

Berryman, E.J., Kutzschbach, M., Trumbull, R.B., Meixner, A., van Hinsberg, V., Kasemann, S.A., and Franz, G. (2017) Tourmaline as a petrogenetic indicator in the Pfitsch Formation, Western Tauern Window, Eastern Alps. Lithos, 284-285, 138-155. http://dx.doi.org/10.1016/j.lithos.2017.04.008

Berryman, E.J., Wunder, B., Rhede, D., Schettler, G., Franz, G., and Heinrich, W. (2016) *P–T–X* controls on Ca and Na distribution between Mg–Al tourmaline and fluid. Contributions to Mineralogy and Petrology, 171, 31. https://doi.org/10.1007/s00410-016-1246-8

Berryman, E.J., Zhang, D.Z., Wunder, B., and Duffy, T.S. (2019) Compressibility of synthetic Mg-Al tourmaline to 60 GPa. American Mineralogist, 104, 1005-1015. https://doi.org/10.2138/am-2019-6967

Birch, F. (1947) Finite elastic strain of cubic cystals. Physical Review, 71, 809-924. https://doi.org/10.1103/PhysRev.71.809

Birch, F. (1978) Finite strain isotherm and velocities for single-crystal and polycrystalline NaCl at high pressures and 300^{o}K. Journal of Geophysical Research-Solid Earth, 83, 1257-1268. https://doi.org/10.1029/JB083iB03p01257

Bosi, F. (2018) Tourmaline crystal chemistry. American Mineralogist, 103, 298-306. https://doi.org/10.2138/am-2018-6289

Bosi, F., and Lucchesi, S. (2007) Crystal chemical relationships in the tourmaline group: Structural constraints on chemical variability. American Mineralogist, 92, 1054-1063. https://doi.org/10.2138/am.2007.2370

Always consult and cite the final, published document. See http:/www.minsocam.org or GeoscienceWorld

This is the peer-reviewed, final accepted version for American Mineralogist, published by the Mineralogical Society of America.
The published version is subject to change. Cite as Authors (Year) Title. American Mineralogist, in press.
DOI: https://doi.org/10.2138/am-2023-9150. http://www.minsocam.org/

Bosi, F., Pezzotta, F., Altieri, A., Andreozzi, G.B., Ballirano, P., Tempesta, G., Cempirek, J., Škoda, R., Filip, J., Čopjaková, R., Novák, M., Kampf, A.R., Scribner, E.D., Groat, L.A., and Evans, R.J. (2022) Celleriite, □$(Mn_2^{2+}Al)Al_6(Si_6O_{18})(BO_3)_3(OH)_3(OH)$, a new mineral species of the tourmaline supergroup. American Mineralogist, 107, 31-42. https://doi.org/10.2138/am-2021-7818

Celata, B., Ballirano, P., Andreozzi, G.B., and Bosi, F. (2021) In situ high‐temperature behaviour of fluor-elbaite: breakdown conditions and products. Physics and Chemistry of Minerals, 48, 24. https://doi.org/10.1007/s00269-021-01147-5

Chakraborty, T. (2021) Tourmaline growth and evolution in S-type granites and pegmatites: constraints from textural, chemical and B-isotopic study from the Gangpur Schist Belt granitoids, eastern India. Geological Magazine, 158(9), 1657-1670. https://doi.org/10.1017/S0016756821000224

Chen, B., Ma, X.H. and Wang, Z.Q. (2014) Origin of the fluorine-rich highly differentiated granites from the Qianlishan composite plutons (South China) and implications for polymetallic mineralization. Journal of Asian Earth Sciences, 93, 301-314. https://doi.org/10.1016/j.jseaes.2014.07.022

Chen, W., Huang, S.J., Ye, Z.L., Song, J.M., Zhang, S.R., Wu, M.Z., Fan, D.W., and Zhou, W.G. (2022) Equation of state of elbaite at high pressure up to 21.1 GPa and room temperature. Physics and Chemistry of Minerals, 49, 27. https://doi.org/10.1007/s00269-022-01201-w

Chen, W., Song, J.M., Huang, S.J., Zhang, S.R., Wu, M.Z., Fan, D.W., and Zhou, W.G. (2023) Thermal expansion behavior of Li-bearing tourmalines investigated by high-temperature synchrotron-based X-ray diffraction. Journal of Physics and Chemistry of Solids, 177, 111278. https://doi.org/10.1016/j.jpcs.2023.111278

Dutrow, B.L., and Henry, D.J. (2011) Tourmaline: A geologic DVD. Elements, 7, 301-306. https://doi.org/10.2113/gselements.7.5.301

Always consult and cite the final, published document. See http:/www.minsocam.org or GeoscienceWorld

This is the peer-reviewed, final accepted version for American Mineralogist, published by the Mineralogical Society of America.
The published version is subject to change. Cite as Authors (Year) Title. American Mineralogist, in press.
DOI: https://doi.org/10.2138/am-2023-9150. http://www.minsocam.org/

Ertl, A., Hughes, J.M., Prowatke, S., Ludwig, T., Lengauer, C.L., Meyer, H.P., Giester, G., Kolitsch, U., and Prayer, A. (2022) Alumino-oxy-rossmanite from pegmatites in Variscan metamorphic rocks from Eibenstein an der Thaya, Lower Austria, Austria: A new tourmaline that represents the most Al-rich end-member composition. American Mineralogist, 107, 157-166. https://doi.org/10.2138/am-2022-8047

Fan, D.W., Kuang, Y.Q., Xu, J.G., Li, B., Zhou, W.G., and Xie, H.S. (2017a) Thermoelastic properties of grossular-andradite solid solution at high pressures and temperatures. Physics and Chemistry of Minerals, 44, 137-147. https://doi.org/10.1007/s00269-016-0843-4

Fan, D.W., Lu, C., Xu, J.G., Yan, B.M., Yang, B., and Chen, J.H. (2017b) Effects of water on P-V-T equation of state of pyrope. Physics of the Earth and Planetary Interiors, 267, 9-18. http://dx.doi.org/10.1016/j.pepi.2017.03.005

Fan, D.W., Xu, J.G., Kuang, Y.Q., Li, X.D., Li, Y.C., and Xie, H.S. (2015a) Compressibility and equation of state of beryl ($Be_3Al_2Si_6O_{18}$) by using a diamond anvil cell and in situ synchrotron X-ray diffraction. Physics and Chemistry of Minerals, 42, 529-539. https://doi.org/10.1007/s00269-015-0741-1

Fan, D.W., Xu, J.G., Ma, M.N., Liu, J., and Xie, H.S. (2015b) P–V–T equation of state of spessartine–almandine solid solution measured using a diamond anvil cell and in situ synchrotron X−ray diffraction. Physics and Chemistry of Minerals, 42, 63-72. https://doi.org/10.1007/s00269-014-0700-2

Fan, D.W., Zhou, W.G., Wei, S.Y., Liu, Y.G., Ma, M.N., and Xie, H.S. (2010) A simple external resistance heating diamond anvil cell and its application for synchrotron radiation X-ray diffraction. Review of Scientific Instruments, 81, 053903. https://doi.org/10.1063/1.3430069

Fei, Y.W., Ricolleau, A., Frank, M., Mibe, K., Shen, G.Y., and Prakapenka, V. (2007) Toward an internally consistent pressure scale. Proceedings of the National Academy of Sciences of the United States of America, 104(22), 9182-9186. https://doi.org/10.1073/pnas.0609013104

Always consult and cite the final, published document. See http:/www.minsocam.org or GeoscienceWorld

This is the peer-reviewed, final accepted version for American Mineralogist, published by the Mineralogical Society of America.
The published version is subject to change. Cite as Authors (Year) Title. American Mineralogist, in press.
DOI: https://doi.org/10.2138/am-2023-9150. http://www.minsocam.org/

Feng, Y.G., Liang, T., Wang, M.X., Zhang, Z., Hao, Y.Y., Cen, J.B., and Dong, Z.Y. (2022) Geochemistry of tourmaline from granitic pegmatites in East Qinling and its implications for mineralization. Acta Petrologica Sinica, 38(2), 428-444. https://doi.org/10.18654/1000-0569/2022.02.08

Filip, J., Bosi, F., Novák, M., Skogby, H., Tuček, J., Čuda, J., and Wildner, M. (2012) Iron redox reactions in the tourmaline structure: High-temperature treatment of Fe^{3+}-rich schorl. Geochima et Cosmochimica Acta, 86, 239-256. http://dx.doi.org/10.1016/j.gca.2012.02.031

Foit, F.F.Jr., Fuchs, Y., and Myers, P.E. (1989) Chemistry of alkali-deficient schorls from two tourmaline-dumortierite deposits. American Mineralogist, 74, 1317-1324.

Fuchs, Y., Lagache, M., and Linares, J. (2002) Annealing in oxidizing conditions of Fe-tourmalines and correlated deprotonation of OH groups. Comptes Rendus Geoscience, 334, 245-249. https://doi.org/10.1016/S1631-0713(02)01755-8

Garofalo, P., Audétat, A., Günther, D., Heinrich, C.A., and Ridley, J. (2000) Estimation and testing of standard molar thermodynamic properties of tourmaline end-members using data of natural samples. American Mineralogist, 85, 78-88.

Gonzalez-Platas, J., Alvaro, M., Nestola, F., and Angel, R. (2016) EosFit7-GUI: A new graphical user interface for equation of state calculations, analyses and teaching. Journal of Applied Crystallography, 49, 1377-1382. https://doi.org/10.1107/S1600576716008050

Gréaux, S., Kono, Y., Nishiyama, N., Kunimoto, T., Wada, K., and Irifune, T. (2011) *P*–*V*–*T* equation of state of $Ca_3Al_2Si_3O_{12}$ grossular garnet. Physics and Chemistry of Minerals, 38, 85-94. https://doi.org/10.1007/s00269-010-0384-1

Guo, M.X., Liu, J.J., Zhai, D.G., Fourestier, J., Liu, M., and Zhu, R. (2023) Tourmaline as an indicator of ore-forming processes: Evidence from the Laodou gold deposit, Northwest China. Ore Geology Reviews, 154, 105304. https://doi.org/10.1016/j.oregeorev.2023.105304

Guo, S., Su, B., John, T., Zhao, K.D., Tang, P., Chen, Y., and Li, Y.B. (2022) Boron release and transfer induced by phengite breakdown in subducted impure

Always consult and cite the final, published document. See http:/www.minsocam.org or GeoscienceWorld

This is the peer-reviewed, final accepted version for American Mineralogist, published by the Mineralogical Society of America.
The published version is subject to change. Cite as Authors (Year) Title. American Mineralogist, in press.
DOI: https://doi.org/10.2138/am-2023-9150. http://www.minsocam.org/

metacarbonates. Lithos, 408-409, 106548. https://doi.org/10.1016/j.lithos.2021.106548

Halama, R., Savov, I.P., Rudnick, R.L., and McDonough, W.F. (2009) Insights into Li and Li isotope cycling and sub-arc metasomatism from veined mantle xenoliths, Kamchatka. Contributions to Mineralogy and Petrology, 158(2), 197-222. https://doi.org/10.1007/s00410-009-0378-5

Hammersley, A.P., Svensson, S.O., Hanfland, M., Fitch, A.N., and Hausermann, D. (1996) Two‐dimensional detector software: From real detector to idealised image or two‐theta scan. High Pressure Research, 14, 235-248. https://doi.org/10.1080/08957959608201408

Han, J.S., Chen, H.Y., Xu, H.J., Nadeau, O., and Xu, C. (2023) Identifying xenocrystic tourmaline in Himalayan leucogranites. American Mineralogist, 108, 1289-1297. https://doi.org/10.2138/am-2022-8615

Hawthorne, F.C., and Henry, D.J. (1999) Classification of the minerals of the tourmaline group. European Journal of Mineralogy, 11(2), 201-215.

Henry, D.J., and Dutrow, B.L. (2012) Tourmaline at diagenetic to low-grade metamorphic conditions: its petrologic applicability. Lithos, 154, 16-32. https://doi.org/10.1016/j.lithos.2012.08.013

Henry, D.J., Novák, M., Hawthorne, F.C., Ertl, A., Dutrow, B.L., Uher, P., Pezzotta, F. (2011) Nomenclature of the tourmaline-supergroup minerals. American Mineralogist, 96, 895-913. https://doi.org/10.2138/am.2011.3636

Henry, D.J., Viator, D., and Dutrow, B.L. (2002) Estimation of light element concentrations in tourmaline: How accurate can it be? Programme with Abstracts of the 18th International Mineralogical Association, 209.

Holland, T.J.B., and Redfern, S.A.T. (1997) Unit cell refinement from powder diffraction data: the use of regression diagnostics. Mineralogical Magazine, 61, 5-77.

Always consult and cite the final, published document. See http:/www.minsocam.org or GeoscienceWorld

This is the peer-reviewed, final accepted version for American Mineralogist, published by the Mineralogical Society of America.
The published version is subject to change. Cite as Authors (Year) Title. American Mineralogist, in press.
DOI: https://doi.org/10.2138/am-2023-9150. http://www.minsocam.org/

Hovis, G.L., Tribaudino, M., Altomare, C., and Bosi, F. (2023) Thermal expansion of minerals in the tourmaline supergroup. American Mineralogist, 108, 1053-1063. https://doi.org/10.2138/am-2022-8580

Hovis, G.L., Tribaudino, M., Leaman, A., Almer, C., Altomare, C., Morris, M., Maksymiw, N., Morris, D., Jackson, K., Scott, B., Tomaino, G., and Mantovani, L. (2021) Thermal expansion of minerals in the pyroxene system and examination of various thermal expansion models. American Mineralogist, 106, 883-899. https://doi.org/10.2138/am-2021-7650

Huang, S.J., Xu, J.G., Chen, C.F., Li, B., Ye, Z.L., Chen, W., Kuang, Y.Q., Fan, D.W., Zhou, W.G., and Ma, M.N. (2020) Topaz, a Potential Volatile-Carrier in Cold Subduction Zone: Constraint from Synchrotron X-Ray Diffraction and Raman Spectroscopy at High Temperature and High Pressure. Minerals, 10, 780. https://doi.org/doi:10.3390/min10090780

Kirkpatrick, P., and Baez, A.V. (1948) Formation of optical images by X-rays. Journal of the Optical Society of America, 38(9), 766-774. https://doi.org/10.1364/JOSA.38.000766

Kim, Y., Jong, K., Li, G., Kim, C., Jon, Y., and Jong, C. (2018) Numerical simulation of intrinsic dipole moment according to ion substitution and order-disorder reactions in tourmaline. Canadian Mineralogist, 56, 951-965. https://doi.org/10.3749/canmin.1800033

Klotz, S., Chervin, J.C., Munsch, P., and Marchand, G.L. (2009a) Hydrostatic limits of 11 pressure transmitting media. Journal of Physics D-Applied Physics, 42, 075413. https://doi.org/10.1107/S0021889806045523

Klotz, S., Paumier, L., Marchand, G.L., and Munsch, P. (2009b) The effect of temperature on the hydrostatic limit of 4:1 methanol-ethanol under pressure. High Pressure Research, 29(4), 649-652. https://doi.org/10.1080/08957950903418194

Konzett, J., Krenn, K., Hauzenberger, C.H., Whitehouse, M., and Hoinkes, G. (2012) High-Pressure Tourmaline Formation and Fluid Activity in Fe-Ti-rich Eclogites from the Kreuzeck Mountains, Eastern Alps, Austria. Journal of Petrology, 53(1), 9-125. https://doi.org/10.1093/petrology/egr057

Always consult and cite the final, published document. See http:/www.minsocam.org or GeoscienceWorld

This is the peer-reviewed, final accepted version for American Mineralogist, published by the Mineralogical Society of America.
The published version is subject to change. Cite as Authors (Year) Title. American Mineralogist, in press.
DOI: https://doi.org/10.2138/am-2023-9150. http://www.minsocam.org/

Kotowski, J., Nejbert, K., and Olszewska-Nejbert, D. (2020) Tourmalines as a Tool in Provenance Studies of Terrigenous Material in Extra-Carpathian Albian (Uppermost Lower Cretaceous) Sands of Miechów Synclinorium, Southern Poland. Minerals, 10, 0917. https://doi.org/10.3390/min10100917

Li, B., Jiang, J.J., Xu, J.G., Tkachev, S.N., Ye, Z.L., Huang, S.J., Guo, W.H., Zeng, Y.J., Prakapenka, V.B., Fan, D.W., and Zhou, W.G. (2022) Effect of Thermoelastic Properties of the Pyrope-Almandine Solid Solutions on the Entrapment Pressure of Garnet-Related Elastic Geobarometer. Frontiers in Earth Science, 9, 833405. https://doi.org/10.3389/feart.2021.833405

Li, B., Xu, J.G., Zhang, D.Z., Ye, Z.L., Huang, S.J., Fan, D.W., Zhou, W.G., Xie, H.S. (2021) Thermoelasticity and stability of natural epidote at high pressure and high temperature: Implications for water transport during cold slab subduction. Geoscience Frontiers, 12, 921-928. https://doi.org/10.1016/j.gsf.2020.05.022

Li, H.J., Qin, S., Zhu, X.P., Liu, J., Li, X.D., Wu, X., and Wu, Z.Y. (2004) In situ high-pressure X-ray diffraction of natural tourmaline. Nuclear Technology, 27(12), 19-922 (in Chinese). https://doi.org/10.3321/j.issn:0253-3219.2004.12.009

Li, J., Huang, X.L., Wei, G.J., Liu, Y., Ma, J.L., Han, L., and He, P.L. (2018) Lithium isotope fractionation during magmatic differentiation and hydrothermal processes in rare-metal granites. Geochimica et Cosmochimica Acta, 240, 64-79. https://doi.org/10.1016/j.gca.2018.08.021

Li, W.B., Qiao, X.Y., Zhang, F.H., and Zhang, L.J. (2022) Tourmaline as a potential mineral for exploring porphyry deposits: a case study of the Bilihe gold deposit in Inner Mongolia, China. Mineralium Deposita, 57, 61-82. https://doi.org/10.1007/s00126-021-01051-6

Likhacheva, A.Y., Rashchenko, S.V., Musiyachenko, K.A., Korsakov, A.V., Collings, I.E., and Hanfland, M. (2019) Compressibility and structure behavior of maruyamaite (K-tourmaline) from the Kokchetav massif at high pressure up to 20 GPa. Mineralogy and Petrology, 113, 613-623. https://doi.org/10.1007/s00710-019-00672-0

Always consult and cite the final, published document. See http:/www.minsocam.org or GeoscienceWorld

This is the peer-reviewed, final accepted version for American Mineralogist, published by the Mineralogical Society of America.
The published version is subject to change. Cite as Authors (Year) Title. American Mineralogist, in press.
DOI: https://doi.org/10.2138/am-2023-9150. http://www.minsocam.org/

Liu, H.Y., Xiao, Y.L., Sun, H., Tong, F.T., Heuser, A., Churikova, T., and Wörner, G. (2020) Trace elements and Li isotope compositions across the Kamchatka arc: Constraints on slab-derived fluid sources. Journal of Geophysical Research-Solid Earth, 125(5), e2019JB019237. https://doi.org/10.1029/2019JB019237

Liu, T., and Jiang, S.Y. (2021) Multiple generations of tourmaline from Yushishanxi leucogranite in South Qilian of western China record a complex formation history from B-rich melt to hydrothermal fluid. American Mineralogist, 106, 994-1008. https://doi.org/10.2138/am-2021-7473

Liu, Y.G., Li, X., Song, H.P., Xu, J.G., Zhang, D.Z., Zhang, J.F., and Wu, X. (2023) Thermal Equation of State of Natural F-Rich Topaz up to 29 GPa and 750 K. Journal of Earth Science, 34(3), 758-766. https://doi.org/10.1007/s12583-021-1418-y

Maloney, J.S., Nabelek, P.I., Sirbescu, M.C., and Halama, R. (2008) Lithium and its isotopes in tourmaline as indicators of the crystallization process in the San Diego County pegmatites, California, USA. European Journal of Mineralogy, 20, 905-916. https://doi.org/10.1127/0935-1221/2008/0020-1823

Meyer, C., Wunder, B., Meixner, A., Romer, R.L., and Heinrich, W. (2008) Boron-isotope fractionation between tourmaline and fluid: an experimental re-investigation. Contributions to Mineralogy and Petrology, 156, 259-267. https://doi.org/10.1007/s00410-008-0285-1

Nabelek, P.I. (2021) Formation of metasomatic tourmalinites in reduced schists during the Black Hills Orogeny, South Dakota. American Mineralogist, 106, 282-289. https://doi.org/10.2138/am-2020-7405

Nakano, T., and Nakamura, E. (2001) Boron isotope geochemistry of metasedimentary rocks and tourmalines in a subduction zone metamorphic suite. Physics of the Earth and Planetary Interiors, 127, 233-252. https://doi.org/10.1016/S0031-9201(01)00230-8

Nishihara, Y., Aoki, I., Takahashi, E., Matsukage, K.N., and Funakoshi, K.I. (2005) Thermal equation of state of majorite with MORB composition. Physics of the

Always consult and cite the final, published document. See http:/www.minsocam.org or GeoscienceWorld

This is the peer-reviewed, final accepted version for American Mineralogist, published by the Mineralogical Society of America.
The published version is subject to change. Cite as Authors (Year) Title. American Mineralogist, in press.
DOI: https://doi.org/10.2138/am-2023-9150. http://www.minsocam.org/

Earth and Planetary Interiors, 148, 73-84. https://doi.org/10.1016/j.pepi.2004.08.003

Novák, M., Povondra, P., and Selway, J.B. (2004) Schorl-oxy-schorl to dravite-oxy-dravite tourmaline from granitic pegmatites; examples from the Moldanubicum, Czech Republic. European Journal of Mineralogy, 16, 323-333. https://doi.org/10.1127/0935-1221/2004/0016-0323

O'Bannon, III. E., Beavers, C.M., Kunz, M., and Williams, Q. (2018) High-pressure study of dravite tourmaline: Insights into the accommodating nature of the tourmaline structure. American Mineralogist, 103, 1622-1633. https://doi.org/10.2138/am-2018-6486

Ogorodova, L.P., Melchakova, L.V., Kiseleva, I.A., and Peretyazhko, I.S. (2004) Thermodynamics of natural tourmaline–elbaite. Thermochimica Acta, 419, 211-214. https://doi.org/10.1016/j.tca.2003.12.019

Ogorodova, L.P., Melchakova, L.V., Kiseleva, I.A., and Peretyazhko, I.S. (2012) Thermodynamics of natural tourmalines—Dravite and schorl. Thermochimica Acta, 539, 1-6. https://doi.org/10.1016/j.tca.2012.03.008

Ota, T., Kobayashi, K., Katsura, T., and Nakamura, E. (2008) Tourmaline breakdown in a pelitic system: Implications for boron cycling through subduction zones. Contributions to Mineralogy and Petrology, 155, 19-32. https://doi.org/10.1007/s00410-007-0228-2

Pezzotta, F., and Laurs, B.M. (2011) Tourmaline: The Kaleidoscopic Gemstone. Elements, 7, 333-338. https://doi.org/10.2113/gselements.7.5.333

Pieczka, A., and Kraczka, J. (2004) Oxidized tourmalines-A combined chemical, XRD and Mössbauer study. European Journal of Mineralogy, 16, 309-321. https://doi.org/10.1127/0935-1221/2004/0016-0309

Qin, F., Wu, X., Zhang, D.Z., Qin, S., and Jacobsen, S.D. (2017) Thermal Equation of State of Natural Ti-Bearing Clinohumite. Journal of Geophysical Research-Solid Earth, 122(11), 8943-8951. https://doi.org/10.1002/2017jb014827

Qiu, K.F., Yu, H.C., Hetherington, C., Huang, Y.Q., Yang, T., and Deng, J. (2021) Tourmaline composition and boron isotope signature as a tracer of

Always consult and cite the final, published document. See http:/www.minsocam.org or GeoscienceWorld

This is the peer-reviewed, final accepted version for American Mineralogist, published by the Mineralogical Society of America.
The published version is subject to change. Cite as Authors (Year) Title. American Mineralogist, in press.
DOI: https://doi.org/10.2138/am-2023-9150. http://www.minsocam.org/

magmatic-hydrothermal processes. American Mineralogist, 106, 1033-1044. https://doi.org/10.2138/am-2021-7495

Slack, J.F. (1996) Tourmaline associations with hydrothermal ore deposits. In Boron: Mineralogy, Petrology and Geochemistry (ES Grew & LM Anovitz, eds.). Reviews in Mineralogy and Geochemistry, 33, 559-644.

Srivastava, P.K., and Singh, P. (2022) Geochemistry of tourmaline of elbaite-dravite series from sapphire bearing pegmatites, proterozoic higher Himalayan Crystalline Complex Jammu and Kashmir, India: Implication for evolution of pegmatite melt. Lithos, 408-409, 106546. https://doi.org/10.1016/j.lithos.2021.106546

Sun, W.D., Ding, X., Hu, Y.H. and Li, X.H. (2007) The golden transformation of the Cretaceous plate subduction in the west Pacific. Earth and Planetary Science Letters, 262(3), 533-542. https://doi.org/10.1016/j.epsl.2007.08.021

Tang, Y.W., Cui, K., Zheng, Z., Gao, J.F., Han, J.J., Yang, J.H., and Liu, L. (2020) LA-ICP-MS U-Pb geochronology of wolframite by combining NIST series and common leadbearing MTM as the primary reference material: implications for metallogenesis of South China. Gondwana Research, 83, 217-231. https://doi.org/10.1016/j.gr.2020.02.006

Tribaudino, M., Hovis, G.L., Almer, C., and Leaman, A. (2022) Thermal expansion of minerals in the amphibole supergroup. American Mineralogist, 107, 1302-1312. https://doi.org/10.2138/am-2022-7988

van Hinsberg, V.J., Henry, D.J., and Marschall, H.R. (2011) Tourmaline: An ideal indicator of its host environment. Canadian Mineralogist, 49, 1-16. https://doi.org/10.3749/canmin.49.1.1

Vincent, V.I., Li, H., Girei, M.B., Förster, M.W., and Kamaunji, V.D. (2023) Tourmaline and zircon trace the nature and timing of magmatic-hydrothermal episodes in granite-related Sn mineralization: Insights from the Libata Sn ore field. American Mineralogist, 108, 552–571. https://doi.org/10.2138/am-2022-8357

Xu, J.G., Fan, D.W., Li, B., Tkachev, S.N., Zhang, D.Z., Yang, G.Z., Zhou, Y., Song, J.M., and Zhou, W.G. (2022a) Thermal equation of state of Cr‑pyrope:

Always consult and cite the final, published document. See http:/www.minsocam.org or GeoscienceWorld

This is the peer-reviewed, final accepted version for American Mineralogist, published by the Mineralogical Society of America.
The published version is subject to change. Cite as Authors (Year) Title. American Mineralogist, in press.
DOI: https://doi.org/10.2138/am-2023-9150. http://www.minsocam.org/

implications for entrapment pressure of Cr-pyrope inclusion in diamond. Contributions to Mineralogy and Petrology, 177, 69. https://doi.org/10.1007/s00410-022-01932-7

Xu, J.G., Fan, D.W., Zhang, D.Z., Guo, X.Z., Zhou, W.G., and Dera, P.K. (2020) Phase Transition of Enstatite-Ferrosilite Solid Solutions at High Pressure and High Temperature: Constraints on Metastable Orthopyroxene in Cold Subduction. Geophysical Research Letters, 47, e2020GL087363. https://doi.org/10.1029/2020GL087363

Xu, J.G., Fan, D.W., Zhang, D.Z., Ma, M.N., Zhou, Y., Tkachev, S.N., and Zhou, W.G., and Dera, P.K. (2022b) Phase Transitions of Fe-, Al- and Ca-Bearing Orthopyroxenes at High Pressure and High Temperature: Implications for Metastable Orthopyroxenes in Stagnant Slabs. Journal of Geophysical Research-Solid Earth, 127, e2021JB023133. https://doi.org/10.1029/2021JB023133

Xu, J.G., Kuang, Y.Q., Zhang, B., Liu, Y.G., Fan, D.W., Li, X.D., and Xie, H.S. (2016) Thermal equation of state of natural tourmaline at high pressure and temperature. Physics and Chemistry of Minerals, 43, 315-326. https://doi.org/10.1007/s00269-015-0796-z

Yavuz, F., Karakaya, N., Yildirim, D.K., Karakaya, M.C., and Kumral, M. (2014) A Windows program for calculation and classification of tourmaline-supergroup (IMA-2011). Computers & Geosciences, 63, 70-87. http://dx.doi.org/10.1016/j.cageo.2013.10.012

Ye, Y., Smyth, J.R., Jacobsen, S.D., and Goujon, C. (2013) Crystal Chemistry, Thermal Expansion, and Raman Spectra of Hydroxyl-Clinohumite: Implications for Water in Earth's Interior. Contributions to Mineralogy and Petrology, 165, 563-574. https://doi.org/10.1007/s00410-012-0823-8

Ye, Z.L., Fan, D.W., Tang, Q.Z., Xu, J.G., Zhang, D.Z., and Zhou, W.G. (2021) Constraining the density evolution during destruction of the lithospheric mantle in the eastern North China Craton. Gondwana Research, 91, 18-30. https://doi.org/10.1016/j.gr.2020.12.001

Always consult and cite the final, published document. See http:/www.minsocam.org or GeoscienceWorld

This is the peer-reviewed, final accepted version for American Mineralogist, published by the Mineralogical Society of America.
The published version is subject to change. Cite as Authors (Year) Title. American Mineralogist, in press.
DOI: https://doi.org/10.2138/am-2023-9150. http://www.minsocam.org/

Ye, Z.L., Li, B., Chen, W., Tang, R.L., Huang, S.J., Xu, J.G., Fan, D.W., Zhou, W.G., Ma, M.N., and Xie, H.S. (2019) Phase transition and thermoelastic behavior of barite-group minerals at high-pressure and high-temperature conditions. Physics and Chemistry of Minerals, 46, 607-621. https://doi.org/10.1007/s00269-019-01026-0

Zack, T., Tomascak, P.B., Rudni, R.L., Dalpé, C., and McDonough, W.F. (2003) Extremely light Li in orogenic eclogites: the role of isotope fractionation during dehydration in subducted oceanic crust. Earth and Planetary Science Letters, 208, 279-290. https://doi.org/10.1016/S0012-821X(03)00035-9

Zhao, Z., Yang, X.Y., Lu, Y.Y., Zhang, Z.Z., Chen, S.S., Sun, C., Hou, Q., Wang, Y., and Li, S. (2022) Geochemistry and boron isotope compositions of tourmalines from the granite-greisen-quartz vein system in Dayishan pluton, Southern China: Implications for potential mineralization. American Mineralogist, 107, 495-508. https://doi.org/10.2138/am-2021-7591

Zhao, M.S., Cai, N., Wang, D.J., and Liu, Q. (2023) Thermal expansivity and high-pressure sound velocities of natural topaz and implications for seismic velocities and H_2O and fluorine recycling in subduction zones. Physics and Chemistry of Minerals, 50, 14. https://doi.org/10.1007/s00269-023-01238-5

Zou, Y., Gréaux, S., Irifune, T., Whitaker, M.L., Shinmei, T., and Higo, Y. (2012) Thermal equation of state of $Mg_3Al_2Si_3O_{12}$ pyrope garnet up to 19 GPa and 1700 K. Physics and Chemistry of Minerals 39, 589-598. https://doi.org/10.1007/s00269-012-0514-z

Always consult and cite the final, published document. See http:/www.minsocam.org or GeoscienceWorld

This is the peer-reviewed, final accepted version for American Mineralogist, published by the Mineralogical Society of America.
The published version is subject to change. Cite as Authors (Year) Title. American Mineralogist, in press.
DOI: https://doi.org/10.2138/am-2023-9150. http://www.minsocam.org/

Figure Captions

Figure 1. Crystal structure of schorl, visualized using the software package CrystalMaker. (Color online)

Figure 2. Representative X-ray diffraction patterns of schorl in this study up to 15.50 GPa and 673 K.

Figure 3. The volumetric compression of schorl, the solid circles represent the data points of schorl in this study, the hollow square represent the data points of schorl from Li et al. (2004), the hollow circles represent the data points of elbaite from Chen et al. (2022), and the solid line was obtained by third-order Birch-Murnaghan EoS fitting of schorl in this study.

Figure 4. The axial compression (a/a_0: black font; c/c_0: red font), the solid circles represent the data points of schorl in this study, the hollow square represent the data points of schorl from Li et al. (2004), the hollow circles represent the data points of elbaite from Chen et al. (2022), and the solid lines were obtained by third-order Birch-Murnaghan EoS fitting of schorl in this study. (Color online)

Figure 5. Volumetric (a) and axial (b and c) Eulerian strain-normalized pressure (F_E-f_E) plot of schorl. The solid lines represent the linear fit through the data.

Figure 6. Unit-cell volume of schorl as a function of pressure and temperature. The solid lines represent isothermal compression curve from fitting High-temperature Birch-Murnaghan EoS at 300, 373, 473, 573, and 673 K with the following parameters: V_0 = 1581.2 ± 0.2 Å^3, K_0 = 110.5 ± 0.6 GPa, K'_0 = 4.6 ± 0.2, $(\partial K_T/\partial T)_P$ = -0.012 ± 0.003 GPa K^{-1} and α_0 = (2.4±0.2) × 10^{-5} K^{-1}. The error bars of the data points are smaller than the symbols.

Figure 7. The variation of K_0 of Fe-bearing tourmalines with Fe content at *Y* site (X_{Fe}, Fe/Fe+Mg+Li+Al). The solid line represents a linear fit to the K_0 values of Fe-bearing tourmalines.

Always consult and cite the final, published document. See http:/www.minsocam.org or GeoscienceWorld

This is the peer-reviewed, final accepted version for American Mineralogist, published by the Mineralogical Society of America.
The published version is subject to change. Cite as Authors (Year) Title. American Mineralogist, in press.
DOI: https://doi.org/10.2138/am-2023-9150. http://www.minsocam.org/

Figure 1

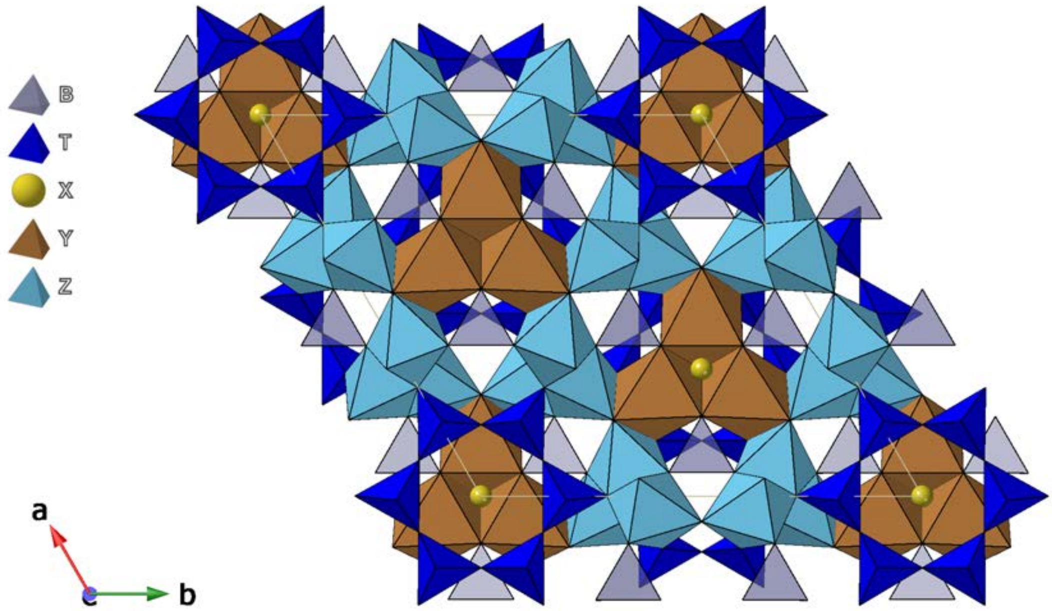

Always consult and cite the final, published document. See http:/www.minsocam.org or GeoscienceWorld

Figure 2

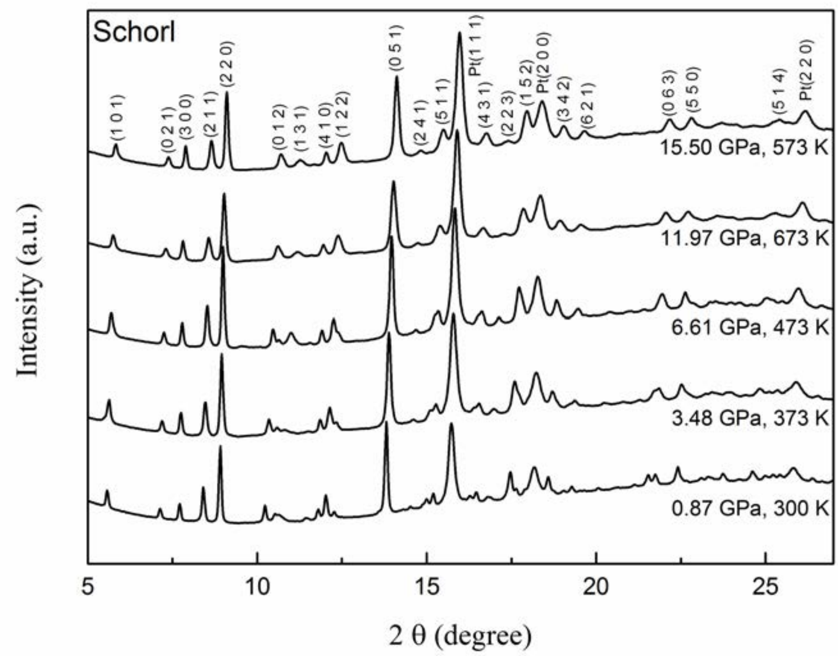
Schorl
(1 0 1)
(0 2 1)
(3 0 0)
(2 1 1)
(2 2 0)
(0 1 2)
(1 3 1)
(4 1 0)
(1 2 2)
(0 5 1)
(2 4 1)
(5 1 1)
Pt(1 1 1)
(4 3 1)
(2 2 3)
(1 5 2)
Pt(2 0 0)
(3 4 2)
(6 2 1)
(0 6 3)
(5 5 0)
(5 1 4)
Pt(2 2 0)
15.50 GPa, 573 K
11.97 GPa, 673 K
6.61 GPa, 473 K
3.48 GPa, 373 K
0.87 GPa, 300 K
Intensity (a.u.)
5
10
15
20
25
2 θ (degree)

This is the peer-reviewed, final accepted version for American Mineralogist, published by the Mineralogical Society of America.
The published version is subject to change. Cite as Authors (Year) Title. American Mineralogist, in press.
DOI: https://doi.org/10.2138/am-2023-9150. http://www.minsocam.org/

Figure 3

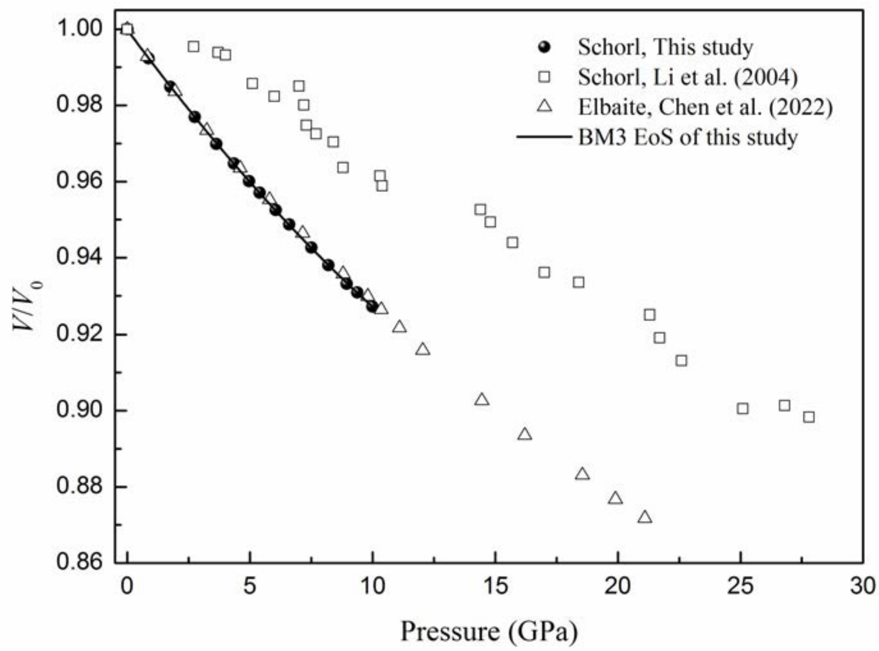

This is the peer-reviewed, final accepted version for American Mineralogist, published by the Mineralogical Society of America.
The published version is subject to change. Cite as Authors (Year) Title. American Mineralogist, in press.
DOI: https://doi.org/10.2138/am-2023-9150. http://www.minsocam.org/

Figure 4

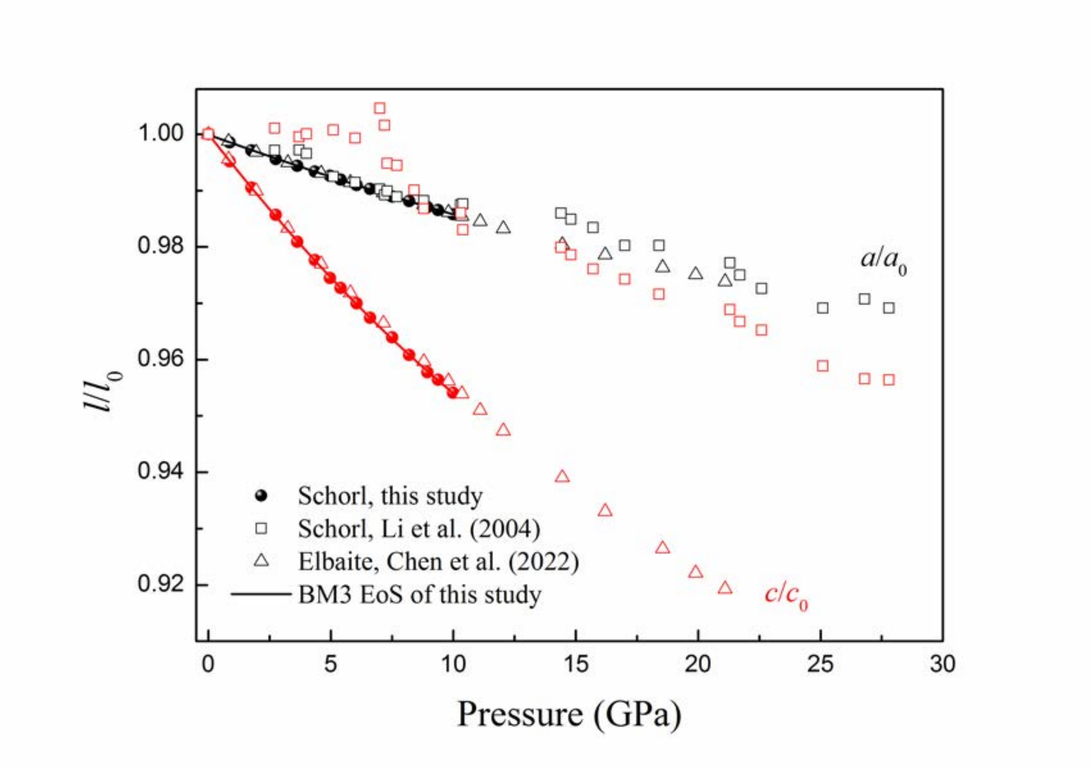

Always consult and cite the final, published document. See http:/www.minsocam.org or GeoscienceWorld

This is the peer-reviewed, final accepted version for American Mineralogist, published by the Mineralogical Society of America.
The published version is subject to change. Cite as Authors (Year) Title. American Mineralogist, in press.
DOI: https://doi.org/10.2138/am-2023-9150. http://www.minsocam.org/

Figure 5

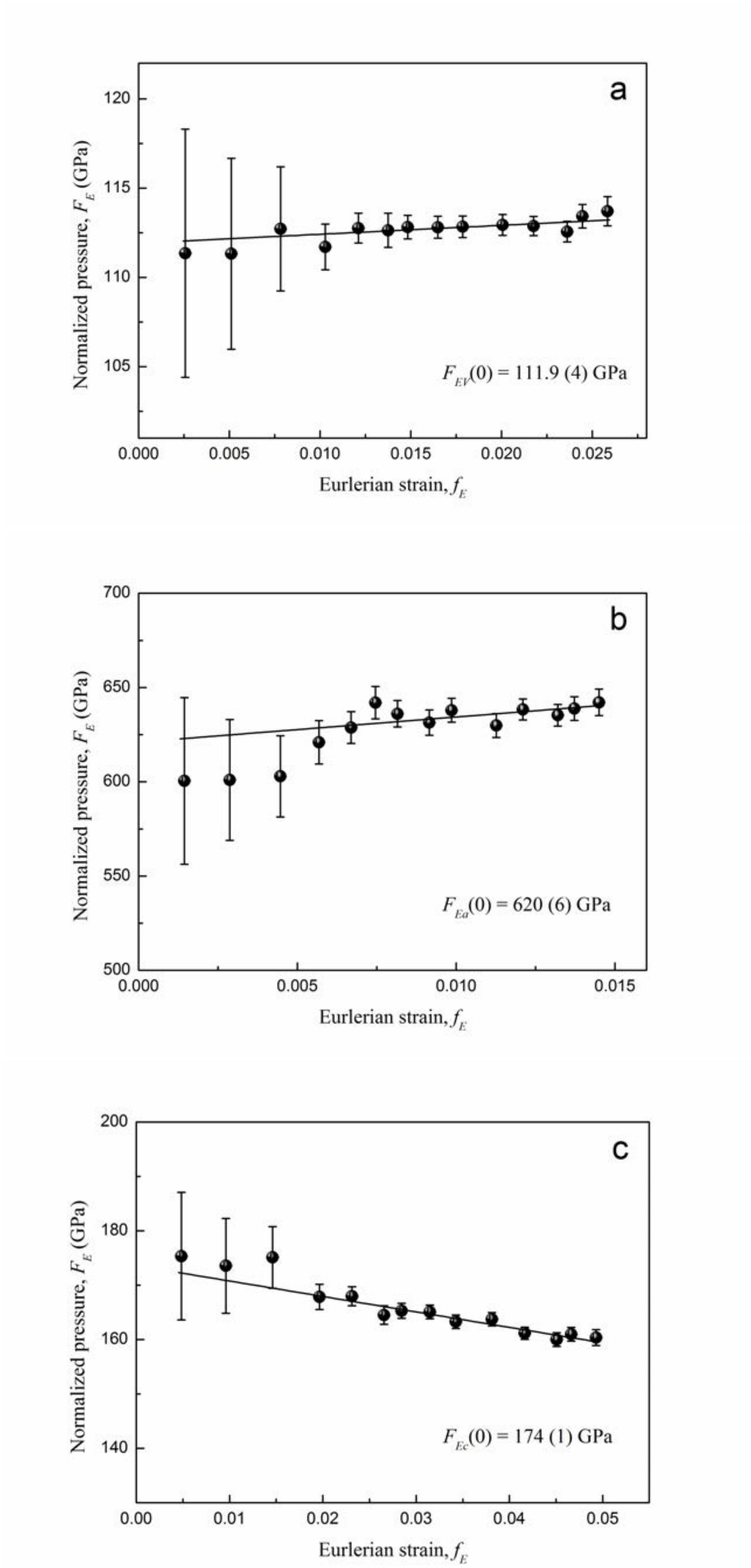

Always consult and cite the final, published document. See http:/www.minsocam.org or GeoscienceWorld

This is the peer-reviewed, final accepted version for American Mineralogist, published by the Mineralogical Society of America.
The published version is subject to change. Cite as Authors (Year) Title. American Mineralogist, in press.
DOI: https://doi.org/10.2138/am-2023-9150. http://www.minsocam.org/

Figure 6

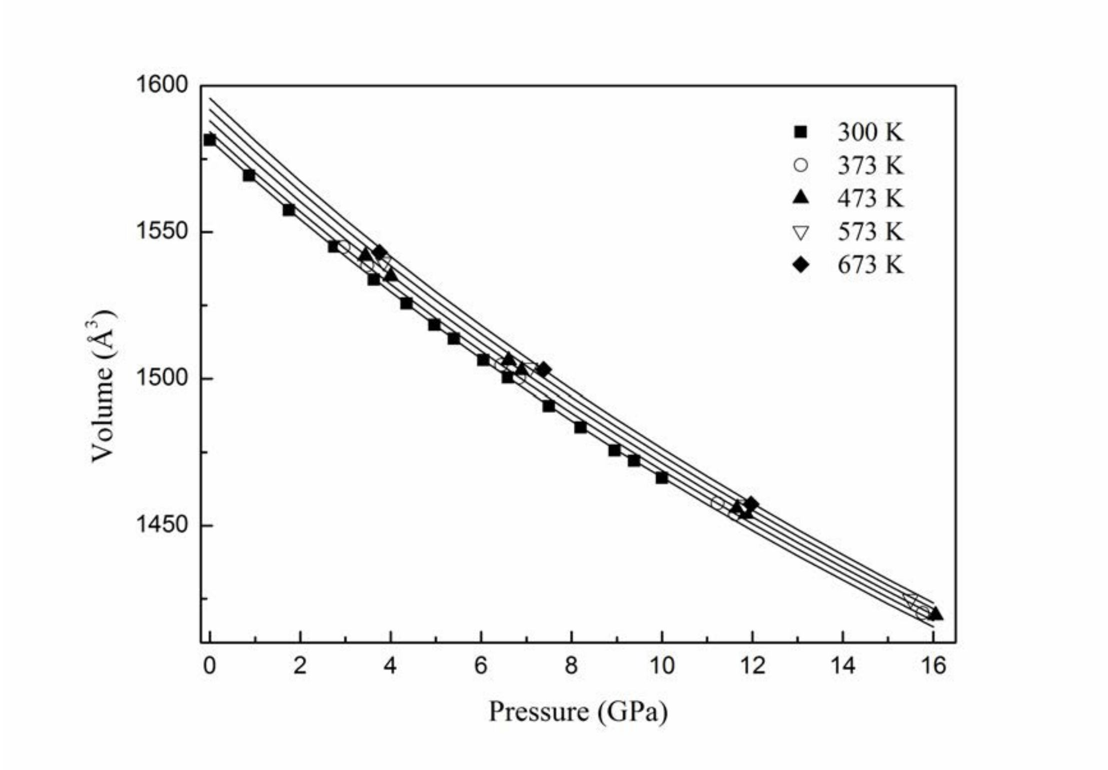

Always consult and cite the final, published document. See http:/www.minsocam.org or GeoscienceWorld

This is the peer-reviewed, final accepted version for American Mineralogist, published by the Mineralogical Society of America.
The published version is subject to change. Cite as Authors (Year) Title. American Mineralogist, in press.
DOI: https://doi.org/10.2138/am-2023-9150. http://www.minsocam.org/

Figure 7

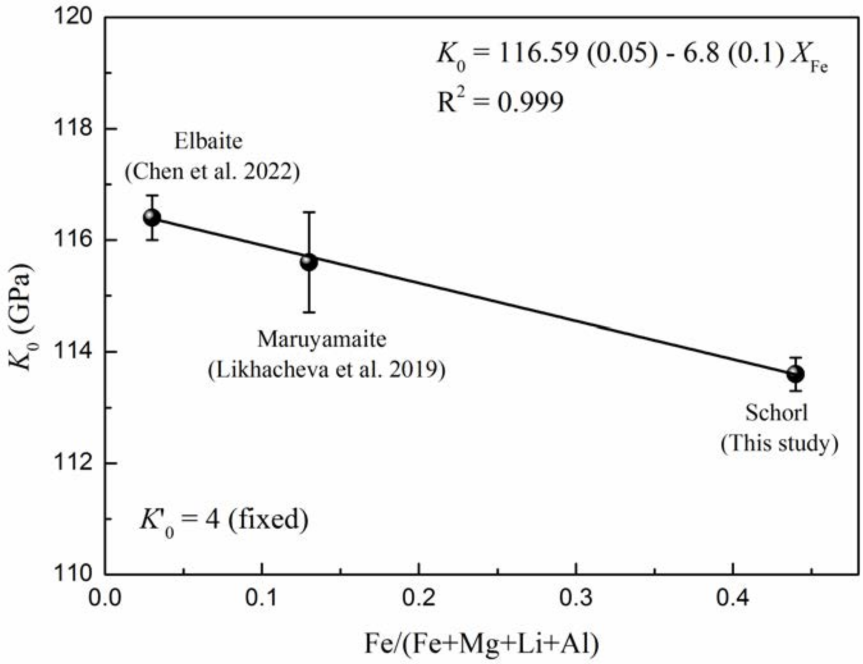

Always consult and cite the final, published document. See http:/www.minsocam.org or GeoscienceWorld

This is the peer-reviewed, final accepted version for American Mineralogist, published by the Mineralogical Society of America.
The published version is subject to change. Cite as Authors (Year) Title. American Mineralogist, in press.
DOI: https://doi.org/10.2138/am-2023-9150. http://www.minsocam.org/

Table 1 Chemical compositions of schorl in this study

Compositions (wt.%) (6)[a]	Schorl
SiO_2	36.03(22)
TiO_2	0.23(3)
Al_2O_3	33.58(31)
B_2O_3*	10.35(27)
Cr_2O_3	0.01(1)
MgO	0.30(7)
FeO[b]	9.35(5)
MnO	0.30(1)
ZnO	0.08(2)
CaO	0.21(1)
Li_2O*	1.09(8)
Na_2O	2.29(5)
K_2O	0.05(1)
P_2O_5	0.01(1)
F	0.05(4)
Total	93.93

Data in the parentheses of compositions represent standard derivations

[a] Number of electron microprobe analyses in parentheses

[b] Total Fe as FeO

* LA-ICP-MS analyses

Always consult and cite the final, published document. See http:/www.minsocam.org or GeoscienceWorld

This is the peer-reviewed, final accepted version for American Mineralogist, published by the Mineralogical Society of America.
The published version is subject to change. Cite as Authors (Year) Title. American Mineralogist, in press.
DOI: https://doi.org/10.2138/am-2023-9150. http://www.minsocam.org/

Table 2 Unit-cell parameters and volumes of schorl at high pressure and room temperature conditions

P (GPa)	*a* (Å) (*Pt*)	*a* (Å)	*c* (Å)	*V* (Å^3)	*a/c*
0.0001	-	15.9532(3)	7.1751(3)	1581.45(5)	2.2234
0.87(5)	3.91904(9)	15.9303(10)	7.1406(11)	1569.3(3)	2.2309
1.75(8)	3.91499(9)	15.9076(12)	7.1071(13)	1557.5(4)	2.2383
2.75(8)	3.91046(9)	15.8825(14)	7.0725(13)	1545.0(5)	2.2457
3.63(3)	3.90655(8)	15.8633(14)	7.0382(13)	1533.8(5)	2.2539
4.35(1)	3.90338(8)	15.8475(13)	7.0147(14)	1525.7(5)	2.2592
4.97(3)	3.90069(9)	15.8355(13)	6.9919(13)	1518.4(5)	2.2648
5.40(1)	3.89885(9)	15.8247(13)	6.9793(13)	1513.6(5)	2.2674
6.05(1)	3.89608(8)	15.8091(14)	6.9595(13)	1506.3(6)	2.2716
6.60(1)	3.89376(9)	15.7983(14)	6.9413(14)	1500.4(6)	2.2760
7.50(1)	3.89001(8)	15.7765(16)	6.9163(15)	1490.8(6)	2.2811
8.20(1)	3.88713(9)	15.7636(15)	6.8937(15)	1483.5(7)	2.2867
8.95(1)	3.88408(8)	15.7467(17)	6.8720(18)	1475.7(7)	2.2914
9.38(3)	3.88235(9)	15.7387(18)	6.8623(17)	1472.1(8)	2.2935
10.00(5)	3.87988(9)	15.7268(20)	6.8456(19)	1466.3(9)	2.2974

Numbers in parenthesis represent standard deviations.

Always consult and cite the final, published document. See http:/www.minsocam.org or GeoscienceWorld

This is the peer-reviewed, final accepted version for American Mineralogist, published by the Mineralogical Society of America.
The published version is subject to change. Cite as Authors (Year) Title. American Mineralogist, in press.
DOI: https://doi.org/10.2138/am-2023-9150. http://www.minsocam.org/

Table 3 Unit-cell volumes of schorl at high pressure and high temperature conditions

P (GPa)	*a* (Å) (*Pt*)	*T* (K)	*a* (Å)	*c* (Å)	*V* (Å^3)
2.96(3)	3.91192(8)	373	15.8835(11)	7.0712(12)	1545.0(1)
3.48(4)	3.90959(7)	373	15.8726(12)	7.0517(13)	1538.6(4)
6.45(8)	3.89666(9)	373	15.8055(11)	6.9546(14)	1504.6(3)
6.84(7)	3.89501(8)	373	15.7977(13)	6.9420(13)	1500.4(4)
11.23(6)	3.87715(8)	373	15.7065(12)	6.8228(16)	1457.6(3)
11.62(6)	3.87562(9)	373	15.6987(13)	6.8122(13)	1453.9(5)
15.77(7)	3.85992(9)	373	15.6247(18)	6.7167(17)	1420.1(8)
3.44(5)	3.91309(9)	473	15.8782(15)	7.0618(15)	1541.9(5)
4.00(6)	3.91057(8)	473	15.8654(12)	7.0414(16)	1535.0(4)
6.61(5)	3.89914(8)	473	15.8075(15)	6.9604(13)	1506.2(6)
6.90(7)	3.89790(9)	473	15.8013(13)	6.9508(14)	1503.0(6)
11.67(6)	3.87836(8)	473	15.7045(18)	6.8171(16)	1456.1(8)
11.86(7)	3.87761(8)	473	15.7006(17)	6.8113(15)	1454.1(8)
16.05(5)	3.86165(8)	473	15.6229(14)	6.7150(16)	1419.4(7)
3.84(8)	3.91464(9)	573	15.8741(16)	7.0558(18)	1539.8(8)
7.08(9)	3.90033(8)	573	15.8022(18)	6.9535(17)	1503.7(8)
11.83(6)	3.88070(8)	573	15.7071(13)	6.8194(13)	1457.0(4)
15.50(4)	3.86651(9)	573	15.6373(12)	6.7285(12)	1424.9(3)
3.75(5)	3.91847(9)	673	15.8804(13)	7.0656(15)	1543.1(5)
7.38(7)	3.90225(8)	673	15.8018(17)	6.9507(15)	1503.1(7)
11.97(5)	3.88315(9)	673	15.7082(14)	6.8199(14)	1457.3(5)

Numbers in parenthesis represent standard deviations.

Always consult and cite the final, published document. See http:/www.minsocam.org or GeoscienceWorld

This is the peer-reviewed, final accepted version for American Mineralogist, published by the Mineralogical Society of America.
The published version is subject to change. Cite as Authors (Year) Title. American Mineralogist, in press.
DOI: https://doi.org/10.2138/am-2023-9150. http://www.minsocam.org/

Table 4 The thermal equation of state parameters of tourmalines

Sample	K_0 (GPa)	K'_0	V_0 (Å^3)	$\alpha V0$ ($\times 10^{-5}$ K^{-1})	$(\partial K/\partial T)_P$ (GPaK^{-1})	References
Schorl	111.6(9)	4.4(2)	1581.45(25)	—	—	This study
	111.6(4)	4.4(1)	1581.45(fixed)	—	—	This study
	113.6(3)	4.0(fixed)	1581.04(20)	—	—	This study
	110.5(6)	4.6(2)	1581.2(2)	2.4(2)	-0.012(3)	This study
	—	—	1581.41(4)	1.61(3)	—	Chen et al. (2023)
Schorl	184(4)	4.0(fixed)	1595.52(198)	—	—	Li et al. (2004)
Elbaite	114.7(7)	4.2(1)	1540.7(6)	—	—	Chen et al. (2022)
	116.4(4)	4.0(fixed)	1540.1(4)	—	—	Chen et al. (2022)
Maruyamaite	112(3)	4.5(4)	1588(1)	—	—	Likhacheva et al. (2022)
	115.6(9)	4.0(fixed)	1587.2(7)	—	—	Likhacheva et al. (2022)
Uvite	96.6(9)	12.5(4)	1537.1(11)	4.39(27)	-0.009(6)	Xu et al. (2016)

Numbers in parenthesis represent standard deviations.

Always consult and cite the final, published document. See http:/www.minsocam.org or GeoscienceWorld

This is the peer-reviewed, final accepted version for American Mineralogist, published by the Mineralogical Society of America.
The published version is subject to change. Cite as Authors (Year) Title. American Mineralogist, in press.
DOI: https://doi.org/10.2138/am-2023-9150. http://www.minsocam.org/

Table 5 The axial compressibility of tourmaline

Sample	K_a (GPa)	K'_a	a_0 (Å)	K_c (GPa)	K'_c	c_0 (Å)	References
Schorl	621(9)	16(3)	15.9532(3)	174(2)	8.7(5)	7.1751(3)	This study
Elbaite [a]	610(8)	20(1)	15.8305(9)	182(1)	8.2(1)	7.0991(9)	Chen et al. (2022)

[a] Refitting using the data presented in Chen et al. (2022). Numbers in parenthesis represent standard deviations.

Always consult and cite the final, published document. See http:/www.minsocam.org or GeoscienceWorld